Monthly Notices
of the
ROYAL ASTRONOMICAL SOCIETY

MNRAS **455,** 3911–3942 (2016) doi:10.1093/mnras/stv2505

Galaxy And Mass Assembly (GAMA): Panchromatic Data Release (far-UV–far-IR) and the low-z energy budget

Simon P. Driver,[1,2★†] Angus H. Wright,[1] Stephen K. Andrews,[1] Luke J. Davies,[1] Prajwal R. Kafle,[1] Rebecca Lange,[1] Amanda J. Moffett,[1] Elizabeth Mannering,[1] Aaron S. G. Robotham,[1] Kevin Vinsen,[1] Mehmet Alpaslan,[3] Ellen Andrae,[4] Ivan K. Baldry,[5] Amanda E. Bauer,[6] Steven P. Bamford,[7] Joss Bland-Hawthorn,[8] Nathan Bourne,[9] Sarah Brough,[6] Michael J. I. Brown,[10] Michelle E. Cluver,[11] Scott Croom,[8] Matthew Colless,[12] Christopher J. Conselice,[7] Elisabete da Cunha,[13] Roberto De Propris,[14] Michael Drinkwater,[15] Loretta Dunne,[9,16] Steve Eales,[16] Alastair Edge,[17] Carlos Frenk,[18] Alister W. Graham,[13] Meiert Grootes,[4] Benne W. Holwerda,[19] Andrew M. Hopkins,[6] Edo Ibar,[20] Eelco van Kampen,[21] Lee S. Kelvin,[5] Tom Jarrett,[22] D. Heath Jones,[23] Maritza A. Lara-Lopez,[24] Jochen Liske,[25] Angel R. Lopez-Sanchez,[6] Jon Loveday,[26] Steve J. Maddox,[9,16] Barry Madore,[27] Smriti Mahajan,[28] Martin Meyer,[1] Peder Norberg,[17,18] Samantha J. Penny,[29] Steven Phillipps,[30] Cristina Popescu,[31] Richard J. Tuffs,[4] John A. Peacock,[9] Kevin A. Pimbblet,[10,32] Matthew Prescott,[11] Kate Rowlands,[2] Anne E. Sansom,[31] Mark Seibert,[27] Matthew W.L. Smith,[15] Will J. Sutherland,[33] Edward N. Taylor,[34] Elisabetta Valiante,[16] J. Antonio Vazquez-Mata,[26] Lingyu Wang,[18,35] Stephen M. Wilkins[26] and Richard Williams[5]

Affiliations are listed at the end of the paper

Accepted 2015 October 26. Received 2015 October 24; in original form 2015 July 16

ABSTRACT

We present the Galaxy And Mass Assembly (GAMA) Panchromatic Data Release (PDR) constituting over 230 deg^2 of imaging with photometry in 21 bands extending from the far-UV to the far-IR. These data complement our spectroscopic campaign of over 300k galaxies, and are compiled from observations with a variety of facilities including: *GALaxy Evolution eXplorer*, Sloan Digital Sky Survey, Visible and Infrared Telescope for Astronomy (VISTA), *Wide-field Infrared Survey Explorer*, and *Herschel*, with the GAMA regions currently being surveyed by VLT Survey Telescope (VST) and scheduled for observations by Australian Square Kilometer Array Pathfinder (ASKAP). These data are processed to a common astrometric solution, from which photometry is derived for ∼221 373 galaxies with $r < 19.8$ mag. Online tools are provided to access and download data cutouts, or the full mosaics of the GAMA regions in each band. We focus, in particular, on the reduction and analysis of the VISTA VIsta Kilo-degree INfrared Galaxy data, and compare to earlier data sets (i.e. 2MASS and UKIDSS) before combining the data and examining its integrity. Having derived the 21-band photometric catalogue, we proceed to fit the data using the energy balance code MAGPHYS. These measurements are then used to obtain the first fully empirical measurement of the 0.1–500 μm energy output of the Universe. Exploring the cosmic spectral energy distribution

★ E-mail: simon.driver@uwa.edu.au
† SUPA, Scottish Universities Physics Alliance.

across three time-intervals (0.3–1.1, 1.1–1.8, and 1.8–2.4 Gyr), we find that the Universe is currently generating $(1.5 \pm 0.3) \times 10^{35}\, h_{70}$ W Mpc^{-3}, down from $(2.5 \pm 0.2) \times 10^{35}\, h_{70}$ W Mpc^{-3} 2.3 Gyr ago. More importantly, we identify significant and smooth evolution in the integrated photon escape fraction at all wavelengths, with the UV escape fraction increasing from 27(18) per cent at $z = 0.18$ in NUV(FUV) to 34(23) per cent at $z = 0.06$. The GAMA PDR can be found at: http://gama-psi.icrar.org/.

Key words: astronomical data bases: miscellaneous – galaxies: evolution – galaxies: general – galaxies: photometry – cosmology: observations.

1 INTRODUCTION

Galaxies are complex systems. At the simplest level ionized gas cools within a dark matter halo (White & Rees 1978), condensing in the densest environments to molecular hydrogen (Shu, Adams & Lizano 1987) which may become self-gravitating and lead to the formation of a stellar population (Bate, Bonnell & Bromm 2003). The stars replenish the interstellar medium through supernovae, winds, and other mass-loss processes (Tinsley 1980; Schoenberner 1983) leading to metal enrichment, dust formation, and the heating of the interstellar medium through shocks and other turbulent processes (McKee & Ostriker 2007, see also Fontanot et al. 2006).

The dust attenuates (through absorption and scattering) a significant portion of the starlight (Calzetti et al. 2000), up to 90 per cent depending on inclination for disc systems (see Driver et al. 2007) and the internal dust geometry and composition. The absorbed fraction of the UV/optical light (highly dependent on morphology but typically 30 per cent for local Universe disc galaxies) is re-radiated at far-infrared (IR) wavelengths (Popescu & Tuffs 2002; Tuffs et al. 2004; Driver et al. 2008). Throughout this process gas is being drawn into the galaxy from the intergalactic medium (IGM; Keres et al. 2005), outflows driven by supernova expel material (Veilleux, Cecil & Bland-Hawthorn 2005), and tidal interactions with neighbouring dark matter haloes may lead to further mass-loss (Toomre & Toomre 1972), or mergers (Lacey & Cole 1993), as well as driving gas to the core leading to re-ignition of the central supermassive black hole (Hopkins et al. 2006). In short, galaxy evolution is governed by a very wide range of complex processes that give rise to multiple energy production and recycling pathways traced from X-ray to radio wavelengths.

Traditionally galaxy surveys have been predominantly single facility campaigns (e.g. the SuperCOSMOS Sky Survey and other Digitised Plate Surveys, Hambly et al. 2001; SDSS, York et al. 2000; 2MASS, Skrutskie et al. 2006; *IRAS*, Soifer, Neugenbauer & Houck 1987; FIRST, White et al. 1997; HIPASS, Barnes et al. 2001) and as a result only capable of exploring a fairly narrow wavelength range. Therefore they often only probe one constituent of this process, e.g. radio surveys which sample the neutral gas content (Barnes et al. 2001), optical campaigns sampling the stellar population (York et al. 2000), and far-IR campaigns sampling the dust emission (Soifer et al. 1987). While panchromatic data sets of relatively modest size have been constructed (e.g. the Spitzer Infrared Nearby Galaxy Survey; Kennicutt et al. 2003), they are generally too small to allow a full exposition of, for example, environment and stellar mass dependences, or subdividing samples to manage co-dependences.

Part of the problem in assembling a *comprehensive* panchromatic catalogue is the range of facilities required, which in many cases are mismatched in sensitivities and resolutions. There are also significant logistical issues: the physics underpinning the energy processes at each wavelength are often very different; the distinct data-streams often have very different wavelength-dependent issues requiring a broad range of specialist skills, and the lack of cooperative global structures to coordinate observations across a suite of facilities which cross international borders. Sampling the full energy range therefore requires cooperation and collaboration across a number of subject areas, the co-operation of time-allocation committees, extensive resources to manage the many data-flows in an optimal way, new techniques to combine the data in a robust manner, and an open skies policy towards final data-products by national and international observatories.

Progress in this area has mainly been driven by technological advancements, coupled with large collaborative efforts, and predominantly in two ways: (1) the construction of increasing samples of well-selected nearby galaxies, often on an object-by-object basis across the wavelength range (e.g. the Atlas of SEDs presented by Brown, Jarrett & Cluver 2014a and the S^{4}G collaboration which now samples over 2000 galaxies, see Sheth et al. 2010 and Munoz-Mateos et al. 2015); or (2) the concerted follow-up of the deep fields observed by the *Hubble Space Telescope* (e.g. the *HST* GOODs, Giavalisco et al. 2004; *HST* COSMOS, Scoville et al. 2007; and *HST* CANDLES, Grogin et al. 2011, and Koekemoer et al. 2011 in particular). In the former the sample sizes are modest (∼100–1000 s of objects), in the latter the galaxies sampled are predominantly at very early epochs (i.e. $z > 1$). In short, no highly complete panchromatic catalogue of the nearby galaxy population exists, suitable for comprehensive statistical analysis, while also covering the full energy range.

The Galaxy And Mass Assembly survey (GAMA; Driver et al. 2009, 2011; Baldry et al. 2010) is an attempt to provide a comprehensive spectroscopic survey (Robotham et al. 2010; Hopkins et al. 2013; Liske et al. 2015) combined with comprehensive panchromatic imaging from the far-UV (FUV) to far-IR and eventually radio. Results to date are based mostly on the spectroscopic campaign combined with the optical imaging to explore structure on kpc to Mpc scales, in particular the GAMA group catalogue (Robotham et al. 2011), the filament catalogue (Alpaslan et al. 2014), and structural studies of galaxy populations (e.g. Kelvin et al. 2014).

Here we introduce the panchromatic imaging which has been acquired, by us or other teams, over the past five years from a variety of ground- and space-based facilities. These surveys collectively provide near-complete sampling of the UV to far-IR wavelength range, through 21 broad-band filters spanning from 0.15–500 μm. The filters represented are: FUV, NUV, *ugriz*, *ZYJHK*$_s$, *W*1, *W*2, *W*3, *W*4, 100, 160, 250, 350, and 500 μm. The contributing surveys in order of increasing wavelength are: the *GALaxy Evolution eXplorer* (*GALEX*) Medium Imaging Survey (MIS; Martin et al. 2005) plus a dedicated campaign (led by RJT), the Sloan Digital Sky Survey

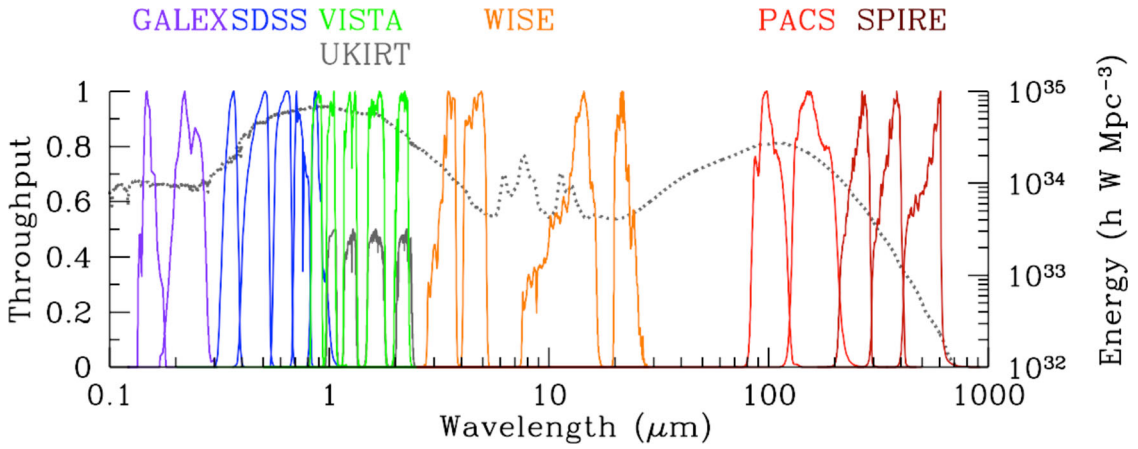

Figure 1. The 21 broad-band combined system throughput curves colour-coded by facility as indicated. Also shown (light grey line) is the recently measured(optical)/predicted(mid and far-IR) CSED derived by Driver et al. (2012). This CSED can be thought of as an energy weighted 'canonical' galaxy SED and highlights how the GAMA PDR filter set samples the key energy regime for nearby and low-redshift galaxies. Note filters are scaled to a peak throughput of 1 except UKIRT which are scaled to 0.5 for clarity.

Data Release 7 (SDSS DR7; Abazajian et al. 2009), the VLT Survey Telescope (VST) Kilo-degree Survey (VST KiDS; de Jong et al. 2013), the VIsta Kilo-degree INfrared Galaxy survey (VIKING; see description of the ESO Public Surveys in Edge et al. 2013), the *Wide-field Infrared Survey Explorer* (*WISE*; Wright et al. 2010), and the Herschel Astrophysical Terahertz Large Area Survey (*Herschel*-ATLAS; Eales et al. 2010). All of these facilities have uniformly surveyed the four largest[1] GAMA regions referred to as G09, G12, G15, and G23 (with only the latter field not covered by SDSS). In the future, the GAMA regions will be surveyed at radio wavelengths by Australian Square Kilometer Array Pathfinder (ASKAP) (as part of the WALLABY or DINGO surveys) and at X-ray wavelengths by eROSITA.

Combined, the four prime GAMA regions cover 230 deg^2 and have uniform spectroscopic coverage to $r_{\rm Petro} < 19.8$ mag (G09, G12, G15) or $i_{\rm Kron} < 19.2$ mag (G23), using a target catalogue constructed from SDSS DR7 (G09, G12, and G15) or VST KiDS (G23) imaging. The original GAMA concept is described in Driver et al. (2009), the tiling algorithm in Robotham et al. (2010), the input catalogue definition in Baldry et al.(2010), the optical/near-IR imaging pipeline in Hill et al. (2011), the spectroscopic pipeline in Hopkins et al. (2013), and the first two data releases including a complete analysis of the spectroscopic campaign and redshift success, in Driver et al. (2011), and Liske et al. (2015), respectively.

One of the scientific motivations is to assemble a comprehensive flux limited sample of ∼221 000 galaxies with near-complete, robust, fully-sampled spectroscopic coverage and robust panchromatic flux measurements from the UV to the far-IR and thereafter apply spectral energy distribution (SED) analysis codes to derive fundamental quantities (e.g. stellar mass, dust mass, opacity, dust temperature, star formation rates etc).

In this paper, we describe the processing and bulk analysis of the panchromatic data and our discussion is divided into three key sections. Section 2 outlines the genesis and unique pre-processing of each imaging data set into a common astrometric mosaic for each region in each band (referred to hereafter as the GAMA SWarps), i.e. homogenization of the data. Section 3 outlines our initial efforts towards combining the various flux measurements from FUV to far-IR which include a combination of aperture-(and seeing)-matched photometry (SDSS/VIKING), table matching (*GALEX*, SDSS/VIKING, *WISE*), curve-of-growth with automated edge detection (*GALEX*), and optical motivated far-IR source detection (SDSS, SPIRE, PACS). In Section 4, we demonstrate and test the robustness of the Panchromatic Data Release (PDR). Finally in Section 5, we provide an empirical measurement of the FUV-far-IR (0.1–500 μm) energy output of the Universe in three volume-limited slices centred at 0.5, 1.5, and 2.5 Gyr in lookback time. Note that by energy output we refer to the energy being generated per Mpc^3 as opposed to the energy flowing through an Mpc^3 (e.g. Driver et al. 2008, 2012; Hill et al. 2010). This is important as the former refers to the instantaneous energy production rate of the Universe (i.e. the luminosity density), whereas the latter is the integrated energy production over all time, including the relic CMB photons (e.g. Domínquez et al. 2011).

Throughout this paper we use $H_0 = 70\ h_{70}$ km s^{-1} Mpc^{-1} and adopt $\Omega_{\rm M} = 0.27$ and $\Omega_\Lambda = 0.73$ (Komatsu et al. 2011). All magnitudes are reported in the AB system.

2 PANCHROMATIC DATA GENESIS

Fig. 1 shows the wavelength grasp of the 21 broad-band filters. The response curves represent the combined system throughputs, normalized to a peak throughput of 1. Also shown as a line (in light grey) is the nearby energy output from the combined $z < 0.1$ galaxy population derived from optical/near-IR analysis of the GAMA data set (see Driver et al. 2012). This highlights how the various bands are sampling the stellar, polycyclic aromatic hydrocarbons, warm (temperature ∼50 K) and cool (temperature ∼20 K) dust emissions of the low-redshift galaxy population (the curve is shown for the energy output at $z = 0$). In this section, we start the process of constructing individual SEDs for every object within the GAMA main survey.

The first step is to place the diverse data on to a common astrometric grid. Table 1 defines the extent of the GAMA PDR regions. We then use the TERAPIX SWARP package (see Bertin 2010) to build single image mosaics for each waveband and each region (see Hill et al. 2011). The SWarp package uses the tangent plane (TAN) World Coordinate System (WCS) to create a gnomic tangent plane projection

[1] GAMA's fifth region, G02, covers 20 deg^2 and overlaps with one of the deep XXM XXL fields, see Liske et al. (2015) for further details.

Table 1. The GAMA panchromatic imaging regions.

GAMA region	SWarp RA centre	SWarp Dec centre	SWarp ΔRA	SWarp Δδ
G09	09:00:30	+00:15:00.0	$19^h15^m24^s$	$7^\circ30'18''$
G12	11:59:30	−00:15:00.0	$19^h15^m24^s$	$7^\circ30'18''$
G15	14:29:30	+00:15:00.0	$19^h15^m24^s$	$7^\circ30'18''$
G23	23:00:00	−32:30:00.0	$14^h00^m00^s$	$6^\circ00'00''$

Note: G02 is not included here but will be described in a dedicated release paper.

Table 2. Key meta-data information of the contributing data sets.

Facility	Data set or survey	Instrument or technique	Filter name	Pivot wavelength	Pixel resolution	Point-source FWHM	Frames supplied	$m_{AB} - m_{Vega}$ (mag)
GALEX	MIS+GO	–	FUV	1535 Å	1.5 arcsec	4.1 arcsec	279	2.16
GALEX	MIS+GO	–	NUV	2301 Å	1.5 arcsec	5.2 arcsec	297	1.67
SDSS	DR7	–	*u*	3557 Å	0.339 arcsec	1.4 arcsec	26 758	0.98
SDSS	DR7	–	*g*	4702 Å	0.339 arcsec	1.4 arcsec	26 758	−0.10
SDSS	DR7	–	*r*	6175 Å	0.339 arcsec	1.4 arcsec	26 758	0.15
SDSS	DR7	–	*i*	7491 Å	0.339 arcsec	1.4 arcsec	26 758	0.38
SDSS	DR7	–	*z*	8946 Å	0.339 arcsec	1.4 arcsec	26 758	0.54
VISTA	VIKING	VIRCAM	*Z*	8800 Å	0.339 arcsec	0.85 arcsec	15 360	0.521
VISTA	VIKING	VIRCAM	*Y*	10 213 Å	0.339 arcsec	0.85 arcsec	15 797	0.618
VISTA	VIKING	VIRCAM	*J*	12 525 Å	0.339 arcsec	0.85 arcsec	34 076	0.937
VISTA	VIKING	VIRCAM	*H*	16 433 Å	0.339 arcsec	0.85 arcsec	15 551	1.384
VISTA	VIKING	VIRCAM	*Ks*	21 503 Å	0.339 arcsec	0.85 arcsec	16 340	1.839
WISE	AllSky	Drizzled	*W*1	3.37 μm	1 arcsec	5.9 arcsec	40	2.683
WISE	AllSky	Drizzled	*W*2	4.62 μm	1 arcsec	6.5 arcsec	40	3.319
WISE	AllSky	Drizzled	*W*3	12.1 μm	1 arcsec	7.0 arcsec	40	5.242
WISE	AllSky	Drizzled	*W*4	22.8 μm	1 arcsec	12.4 arcsec	40	7.871
Herschel	ATLAS	PACS	100 μm	101 μm	3 arcsec	9.6 arcsec	4 (and 1 for G23)	N/A
Herschel	ATLAS	PACS	160 μm	161 μm	4 arcsec	12.5 arcsec	4 (and 1 for G23)	N/A
Herschel	ATLAS	SPIRE	250 μm	249 μm	6 arcsec	18 arcsec	4 (and 1 for G23)	N/A
Herschel	ATLAS	SPIRE	350 μm	357 μm	8 arcsec	25 arcsec	4 (and 1 for G23)	N/A
Herschel	ATLAS	SPIRE	500 μm	504 μm	12 arcsec	36 arcsec	4 (and 1 for G23)	N/A

centred on the coordinates shown in Table 1. One might argue about the merit of constructing such large SWarped images (∼110 deg^2 each or up to 80 GB for SDSS/VIKING data); however, it was decided that this was preferable to managing the ∼1 million non-aligned boundaries across the PDR. Taking each facility in turn we now describe the pre-processing necessary to construct our GAMA SWarps. Note that in addition to the native-resolution SWarps (see Table 2), we also construct a set of SWarps at a common 3.39 arcsec resolution (i.e. 10 times the VISTA pixel scale) for later use in deriving coverage flags and background noise estimations.

2.1 *GALEX* MIS, GO, and archive data

The *GALEX* (Martin et al. 2005) was a medium-class explorer mission operated by NASA and launched on 2003 April 28. The satellite conducted a number of major surveys and observer motivated programmes, most notably the all-sky imaging survey (typically 200 s integrations per tile) and the MIS (typically 1500 s per tile). The *GALEX* satellite is built around a 0.5-m telescope with a field-of-view of 1.13 deg^2, a pixel resolution of 1.5 arcsec, and a point spread function (PSF) full width at half-maximum (FWHM) of 4.2 and 5.3 arcsec in the FUV (153 nm) and NUV (230 nm) bands, respectively (Morrissey et al. 2007). Imaging data sampled at 1.5 arcsec from V7 of the *GALEX* pipeline forms the basis for constructing the SWarped images. At the time of commencement of the GAMA survey, the GAMA regions contained patchy coverage with *GALEX*. A dedicated programme led by one of us (RJT), was pursued providing further *GALEX* observations to MIS depth (1500 s) and completed in 2013 April (using funds raised from the GAMA and *Herschel*-ATLAS Consortium to reactivate and extend the *GALEX* mission). The final collated data provide near-complete NUV and FUV coverage of the four primary GAMA regions. Due to the failure of the FUV channel mid-mission, the coverage at FUV in G23 is poor. However in G09, G12, and G15, coverage is at the 90 per cent level in both bands (of which almost all is at MIS depth in the NUV, and 60 per cent is at MIS depth in the FUV, see Section 2.6).

The analysis of the various *GALEX* data sets are described in detail in Andrae (2014) and summarized in Liske et al. (2015), and result in background subtracted intensity maps scaled to the common *GALEX* zero-points (Table 3). As the data originate from a variety of sources the exposure time is variable (see Fig. 2). To create our SWarps, we take all available *GALEX* data frames with exposure times greater than 800 s. Within the PDR only *GALEX* has such variable integration times.

In building the SWarps, a common circular mask (of radius 35 arcmin) was used to trim the outer ∼5 per cent of the image edges where the data quality degrades due to the vignetting of the

Table 3. Surface brightness limits of our GAMA SWarp set (FUV to mid-IR).

SWarp Facility/Filter/Field	Zero-Pp (AB mag for 1ADU)	SWarp mean (arcsec^{-1})	$1\sigma_{\rm Sky}$ (mag arcsec^{-2})[a]	5σ limit (mag)[b]	5σ limit (Jy)[c]	Coverage (%)
GALEX FUV G09	18.82	0.000 148	28.41	25.23	2.94$E-07$	88
GALEX FUV G12	18.82	5.04$E-05$	29.58	26.40	1$E-07$	92
GALEX FUV G15	18.82	0.000 13	28.54	25.37	2.59$E-07$	95
GALEX FUV G23	18.82	0.000 266	27.77	24.59	5.31$E-07$	75
GALEX NUV G09	20.08	0.001 25	27.35	23.92	9.84$E-07$	94
GALEX NUV G12	20.08	0.001 16	27.43	23.99	9.17$E-07$	97
GALEX NUV G15	20.08	0.001 61	27.07	23.64	1.27$E-06$	95
GALEX NUV G23	20.08	0.001 09	27.50	24.07	8.58$E-07$	99
SDSS *u* G09	30.00	142	24.61	22.24	4.61$E-06$	100
SDSS *u* G12	30.00	163	24.47	22.09	5.28$E-06$	100
SDSS *u* G15	30.00	156	24.51	22.14	5.06$E-06$	100
SDSS *g* G09	30.00	54.3	25.66	23.29	1.76$E-06$	100
SDSS *g* G12	30.00	65.3	25.46	23.09	2.12$E-06$	100
SDSS *g* G15	30.00	62.6	25.50	23.13	2.03$E-06$	100
SDSS *r* G09	30.00	76.7	25.28	22.91	2.49$E-06$	100
SDSS *r* G12	30.00	95.4	25.05	22.67	3.09$E-06$	100
SDSS *r* G15	30.00	90.5	25.10	22.73	2.93$E-06$	100
SDSS *i* G09	30.00	116	24.84	22.47	3.75$E-06$	100
SDSS *i* G12	30.00	140	24.62	22.25	4.56$E-06$	100
SDSS *i* G15	30.00	129	24.72	22.35	4.19$E-06$	100
SDSS *z* G09	30.00	506	23.23	20.86	1.65$E-05$	100
SDSS *z* G12	30.00	579	23.09	20.71	1.88$E-05$	100
SDSS *z* G15	30.00	556	23.13	20.76	1.81$E-05$	100
VIKING *Z* G09	30.00	59.8	25.55	23.18	1.94$E-06$	100
VIKING *Z* G12	30.00	60.6	25.54	23.17	1.97$E-06$	100
VIKING *Z* G15	30.00	62	25.51	23.14	2.01$E-06$	99
VIKING *Z* G23	30.00	67.9	25.41	23.04	2.2$E-06$	100
VIKING *Y* G09	30.00	123	24.77	22.40	3.98$E-06$	100
VIKING *Y* G12	30.00	110	24.89	22.52	3.56$E-06$	100
VIKING *Y* G15	30.00	111	24.88	22.51	3.61$E-06$	100
VIKING *Y* G23	30.00	129	24.71	22.34	4.2$E-06$	100
VIKING *J* G09	30.00	167	24.44	22.06	5.43$E-06$	100
VIKING *J* G12	30.00	161	24.48	22.10	5.23$E-06$	100
VIKING *J* G15	30.00	146	24.58	22.21	4.74$E-06$	100
VIKING *J* G23	30.00	155	24.52	22.14	5.04$E-06$	100
VIKING *H* G09	30.00	329	23.70	21.33	1.07$E-05$	98
VIKING *H* G12	30.00	302	23.79	21.42	9.82$E-06$	99
VIKING *H* G15	30.00	313	23.75	21.38	1.02$E-05$	97
VIKING *H* G23	30.00	325	23.71	21.34	1.06$E-05$	100
VIKING *K* G09	30.00	332	23.69	21.32	1.08$E-05$	100
VIKING *K* G12	30.00	337	23.67	21.30	1.09$E-05$	100
VIKING *K* G15	30.00	303	23.79	21.42	9.83$E-06$	100
VIKING *K* G23	30.00	285	23.86	21.48	9.25$E-06$	100
*WISE W*1 G09	23.18	0.262	24.64	21.09	1.33$E-05$	100
*WISE W*1 G12	23.18	0.281	24.56	21.01	1.43$E-05$	100
*WISE W*1 G15	23.14	0.21	24.84	21.29	1.11$E-05$	100
*WISE W*1 G23	23.14	0.187	24.96	21.41	9.9$E-06$	100
*WISE W*2 G09	22.82	0.327	24.04	20.38	2.55$E-05$	100
*WISE W*2 G12	22.82	0.367	23.91	20.26	2.87$E-05$	100
*WISE W*2 G15	22.82	0.264	24.27	20.61	2.06$E-05$	100
*WISE W*2 G23	22.82	0.229	24.42	20.77	1.79$E-05$	100
*WISE W*3 G09	23.24	2.33	22.32	18.59	0.000 133	100
*WISE W*3 G12	23.24	2.68	22.17	18.44	0.000 153	100
*WISE W*3 G15	23.24	1.77	22.62	18.89	0.000 101	100
*WISE W*3 G23	23.24	2.18	22.39	18.66	0.000 125	100
*WISE W*4 G09	19.60	0.278	20.99	16.64	0.000 802	100
*WISE W*4 G12	19.60	0.305	20.89	16.54	0.000 879	100
*WISE W*4 G15	19.60	0.208	21.31	16.96	0.000 599	100
*WISE W*4 G23	19.60	0.265	21.05	16.69	0.000 762	100
PACS 100 G09	8.90	0.000 562	–	12.96	0.0894	100
PACS 100 G12	8.90	0.000 545	–	12.99	0.0879	100
PACS 100 G15	8.90	0.000 547	–	12.99	0.0863	100

Table 3 – *continued.*

SWarp Facility/Filter/Field	Zero-point (AB mag for 1ADU)	SWarp mean (arcsec^{-1})	$1\sigma_{\rm Sky}$ (mag arcsec^{-2})[a]	5σ limit (mag)[b]	(Jy)[c]	Coverage (%)
PACS 100 G23	8.90	0.000 476	–	13.14	0.0795	100
PACS 160 G09	8.90	0.000 278	–	13.44	0.103	100
PACS 160 G12	8.90	0.000 273	–	13.46	0.101	100
PACS 160 G15	8.90	0.000 271	–	13.47	0.101	100
PACS 160 G23	8.90	0.000 227	–	13.66	0.0903	100
SPIRE[d] 250 G09	11.68	0.000 759	–	12.56	0.0343	80
SPIRE[d] 250 G12	11.68	0.000 73	–	12.60	0.0330	81
SPIRE[d] 250 G15	11.68	0.000 73	–	12.59	0.0333	84
SPIRE[d] 250 G23	11.68	0.000 885	–	12.52	0.0357	100
SPIRE[d] 350 G09	11.67	0.000 447	–	12.36	0.0412	80
SPIRE[d] 350 G12	11.67	0.000 424	–	12.41	0.0394	81
SPIRE[d] 350 G15	11.67	0.000 423	–	12.41	0.0393	84
SPIRE[d] 350 G23	11.67	0.000 518	–	12.51	0.0357	100
SPIRE[d] 500 G09	11.62	0.000 228	–	12.16	0.0495	80
SPIRE[d] 500 G12	11.62	0.000 217	–	12.23	0.0467	81
SPIRE[d] 500 G15	11.62	0.000 221	–	12.21	0.0476	84
SPIRE[d] 500 G23	11.62	0.000 257	–	12.17	0.0490	100

Notes. [a] $\mu_{1\sigma} = ZP - 2.5\log_{10}(\sigma_{\rm ADU})$.
[b] $5\sigma{\rm limit} = {\rm ZP} - 2.5\log_{10}(5\sqrt{\pi{\rm HWHM}^2}\sigma_{\rm ADU})$, where HWHM is Half Width Half-Maximum of the seeing-disc (i.e. 0.5 FWHM).
[c] $F_\nu({\rm Jy}) = 3631 \times 10^{-0.4{\rm mag}_{5\sigma{\rm limit}}}$.
[d] SPIRE maps are in units of Jansky per beam and to generate these zero-points we have added a factor of $2.5\log_{10}(B/N^2)$, where B is the beam size given as 466, 821, and 1770 arcsec^2 in 250, 350, and 500 μm, respectively, and N is the pixel size given in Table 2.

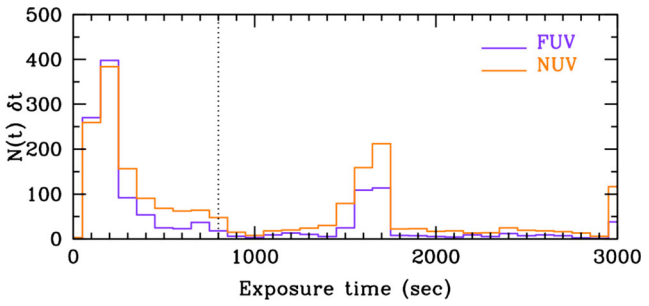

Figure 2. The distribution of exposure times contributing to the final FUV and NUV SWarps. The dotted vertical denotes the cutoff below which frames are not used in the final SWarps.

telescope aperture (see Morrissey et al. 2007 and also Drinkwater et al. 2010, who adopted a similar radius for the WiggleZ survey). In total we have 150, 137, 175, and 22 *GALEX* pointings in FUV and 167, 175, 176, and 133 in the NUV for G09, G12, G15, and G23, respectively. These are combined to produce single image SWarps at the FUV and NUV native resolution for each region.

Note that a particular subtlety in building the FUV and NUV SWarps is the nature of the sky backgrounds. In the FUV, the majority of pixels have zero flux (i.e. sky values of <1 photon) and hence the distribution of sky pixel-values is highly asymmetrical (i.e. Poissonian). Great care was taken by the GAMA *GALEX* team (MS, RJT, EA) to model and remove the backgrounds for each individual frame appropriately and provide to GAMA background subtracted FUV data (see Liske et al 2015, Section 4.2 for further details). Hence when constructing the FUV SWarps the background subtraction option was switched off. Furthermore care should be taken in further background analysis of *GALEX* FUV data by only using mean statistics and not median statistics because of the highly asymmetrical background distribution, and ensuring sufficient counts within any aperture to derive a robust mean. The NUV data have a significant sky signal and is therefore processed with the SWarp background subtraction on using a 128 × 128 pixel mesh (i.e. 198 arcsec × 198 arcsec).

2.2 SDSS DR7

The Sloan Digital Sky Survey (SDSS; York et al. 2000) provides uniform optical imaging of the G09, G12, and G15 regions in *ugriz* bands at 0.4 arcsec pixel resolution with a typical PSF FWHM of 1.4 arcsec (see Hill et al. 2011, fig. 3). As the GAMA spectroscopic survey was predicated on the SDSS imaging (Baldry et al. 2010) there is by design uniform *ugriz* coverage of the three equatorial GAMA regions (G09, G12, and G15). In due course these regions, along with G23, are being surveyed by the KiDS team which will provide both deeper (2 mag) and higher (×2) spatial resolution data (see de Jong et al. 2013).

Here, we re-utilize the large mosaic GAMA SWarps built from the SDSS DR7 (Abazajian et al. 2009) by Hill et al. (2011, see update in Liske et al. 2015). In brief, this involved the construction of both native seeing SWarps and SWarps built from data frames convolved to a uniform 2 arcsec FWHM. The starting point is to download all contributing SDSS frames from the DR7 data base, measure the PSF using PSFEX (Bertin et al. 2011), renormalize the data to a common zero-point, and produce both native seeing and convolved data frames (using FGAUSS within HEASOFT to produce a common PSF FWHM of 2 arcsec). We then build SWarps at both the native and convolved resolutions from the distinct renormalized data frames. During the SWarping process (see Bertin 2010; Hill et al. 2011), the sky background is subtracted using a coarse 512 × 512 pixel median filter to create a grid which in turn is median filtered 3 × 3 before being fitted by a bi-cubic spline to represent the background structure. The use of a large initial median filter is to ensure minimal degradation of the photometry and shapes of extended systems.

G23 lies too far south to be observed by SDSS but along with G09, G12, and G15 are being observed to a uniform depth within

the KiDS survey. The analysis of the KiDS data for GAMA and the preparation of the input catalogue for G23 will be presented in Moffett et al. (2015). At the present time optical SWarps for G23 do not exist.

2.3 VISTA VIKING

The Visible and Infrared Telescope for Astronomy (VISTA; Sutherland et al. 2015) is a 4.1 m short focal length IR optimized survey telescope located 1.5 km from the VLT telescopes at Paranal Observatory. VISTA is owned and operated by ESO and commenced operations on 2009 December 11. VISTA then entered a five year period of survey operation to conduct a number of ESO Public Surveys (Arnaboldi et al. 2007). One of these surveys, the VIsta Kilodegree INfrared Galaxy Survey (VIKING), will cover 1500 deg^2 in two contiguous regions located in the north and south Galactic caps plus the G09 region. During the first two years of operations the VIKING survey prioritized the GAMA and *Herschel*-ATLAS survey regions. The VIKING survey footprint therefore covers all four primary GAMA regions (by design), in five pass bands ($ZYJHK_s$) at sub-arsecond resolution to projected 5σ point-source sensitivities of 23.1, 22.3, 22.1, 21.5, 21.2 AB mag (respectively).

The near-IR camera (VIRCAM; Dalton et al. 2006) consists of 16 Raytheon VIRGO HgCdTe arrays (detectors) sampling an instantaneous field-of-view of 0.6 deg^2 within the 1.65 deg diameter field. In routine operation a set of microdithered and stacked frames are formed, which are referred to as PAW-PRINTS. The on-camera dither sequence does not cover the gaps between the detectors and hence a sequence of six interleaved PAW-PRINTS is required to produce a contiguous coverage rectangular TILE of 1.475 deg $\times$ 1.017 deg.

PAW-PRINT data from the VISTA telescope is pipeline processed (Lewis, Irwin & Bunclark 2010) by the Cambridge Astronomy Survey Unit (CASU) to produce astrometrically and photometrically calibrated data. This process includes flat-fielding, bias subtraction, and linearity corrections. The PAW-PRINTS are then transmitted to the Wide Field Astronomy Unit (WFAU) at the Royal Observatory Edinburgh. The WFAU combines the PAW-PRINTS into the TILES which are then served to the community through both the ESO archive and the UK VISTA Science Archive. As the stacked TILE data does not include sky-subtraction, sharp discontinuities can be introduced into the TILES. An additional concern is that the TILES may be constructed from PAW-PRINTS taken during significantly different seeing conditions. As we wish to both sky-subtract and homogenize the PSF to allow for aperture-matched photometry (see Hill et al. 2011), we requested access to all the VIKING PAW-PRINT data provided to the WFAU from CASU, which lay within the GAMA primary regions. This consisted of 9269 Rice compressed multi-extension FITS files (v1.3 data from the CASU archive). These data were expanded out as individual detectors resulting in 148 304 individual frames. Properties were extracted from the headers for each detector (airmass, extinction, exposure time, zero-point, sky level, seeing) and the seeing measured directly using PSFEX (Bertin et al. 2011). The data for each individual detector were then rescaled to a common zero-point (30) using equation (1):

$$I_{\rm New} = I_{\rm Old} 10^{(-0.4(Z-2.5\log_{10}(1/t)-(\tau(\sec\chi-1))+X_{\rm V.AB}-30))}, \quad (1)$$

where Z is the quoted zero-point, t is the exposure time in seconds, τ is the extinction in the relevant band and sec χ is the airmass. These values are obtained directly from the FITS headers post-CASU processing. $X_{\rm V.AB}$ is the conversion from Vega to AB magnitudes (i.e. 0.521, 0.618, 0.937, 1.384 or 1.839 for Z,Y,J,H,K, respectively) and were derived by CASU from the convolution of the complete system response functions convolved with the spectrum of Vega and a flat AB spectrum. The response functions in comparison to those for UKIRT are shown in Fig. 1.

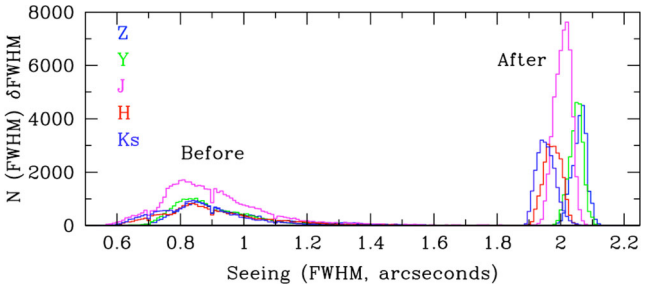

Figure 3. Pre- and post-convolution seeing measurements of the 148 304 VISTA VIKING frames using PSFEX.

These data were convolved with the Gaussian kernel required to produce an FWHM of 2 arcsec by assuming the PSF can be described as a Gaussian and that the convolution of two Gaussians produces a broader Gaussian, i.e. in line with our convolved SDSS data (see Hill et al. 2011). Fig. 3 shows the pre- and post-convolved FWHM as measured by PSFEX. As can be seen the original seeing is predominantly sub-arcsecond as expected from the ESO Paranal (NTT peak) site and all the data lie well below our desired target PSF FWHM of 2 arcsec. Because the data are so much better than the target PSF FWHM value the assumption of a Gaussian profile should produce near-Gaussian final PSFs. Note that the J-band data are observed twice, increasing the abundance of independent measurements. The post-processed data are centred close to the target PSF FWHM of 2 arcsec with some indication of slight systematics between the bands at the 5 per cent level. Note this is not a major concern as we use apertures with minimum major or minor diameters of 5 arcsec when measuring our $u-K_s$ aperture-matched photometry (see Section 3.1).

From our initial SWarps, we noted that a portion of data is clearly of very low quality (see Fig. 4). We therefore elected to inspect a subset of the data by selecting three categories: OUTLIERS defined as those with seeing better than 0.5 arcsec or worse than 1.5 arcsec, a zero-point multiplier of greater than 40, a sky value of less than 100 ADU counts or a CASU TILECODE not equal to 0, 56, or -1, i.e. 9535 frames in total; CONTROL defined as a random set of 1000 frames not included in the above selection; and SPARSE defined as every detector eight frame not already included in one of the earlier samples, i.e. 6945 frames. These 16 590 frames were inspected by two of us (SPD, AHW) using the MOGRIFY routine within the IMAGEMAGICK package to generate grey-scale images where the lowest 2 per cent of data were set black, the highest 10 per cent white, and with histogram equalization in-between. This scaling amplifies background gradients rendering even the best quality data in the poorest light (see Fig. 4). We then rejected or accepted the frames via visual inspection and attempted to identify a measurable quantity which best separated out the rejected frames, see Fig. 5. This resulted in the adoption of a simple cut on the zero-point multiplier factor, whereby all frames which require a rescaling of $\times$ 30 or more are rejected in addition to those already identified from the visual inspections. In total 3262 of our 148 304 frames were rejected (i.e. 2.2 per cent of the data). Examples of accepted and rejected frames are shown in Fig. 4 and common causes are bright sky, detector failures and telescope pointing errors.

The remaining frames were then SWarped (Bertin et al. 2010) to the GAMA PDR regions specified in Table 1 with a pixel size of

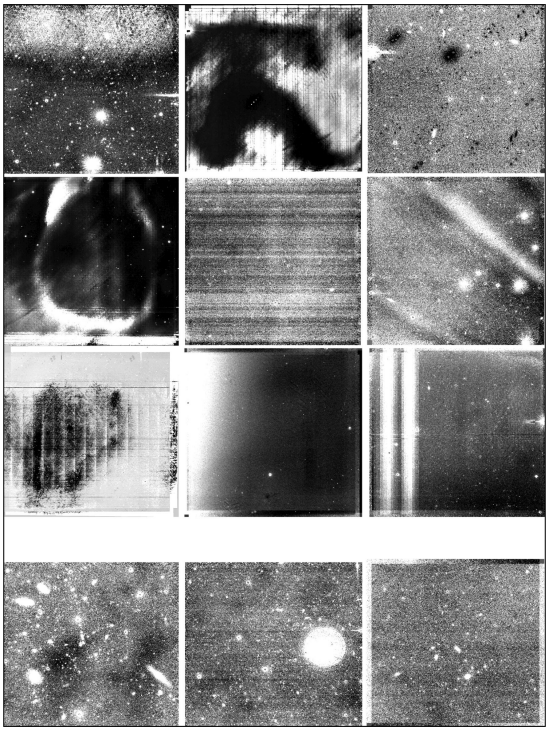

Figure 4. Examples of poor quality (top three rows) and acceptable quality (bottom row) VIKING frames. Approximately 12 per cent of the VIKING data were visually inspected based on outlying values in airmass, sky background, zero-point, and seeing.

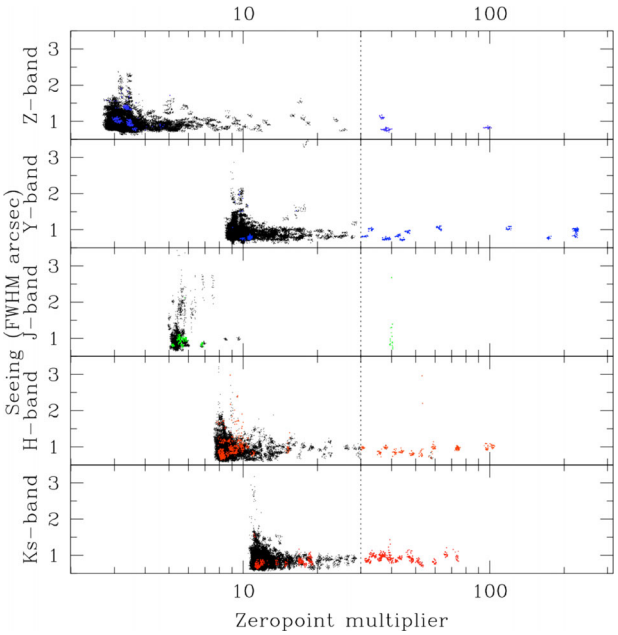

Figure 5. Seeing versus zero-point multiplier for each band (as indicated). A cut of 30 appears to isolate the majority of low-quality frames (indicated by the coloured points).

0.339 arcsec using the TAN WCS projection. During the SWarping process the background for each contributing detector was removed using a 128 × 128 pixel median filter which in turn was median filtered by a 3 × 3 grid before being fitted with a bi-cubic spline. The choice of background filter size is critical; too high and the structure

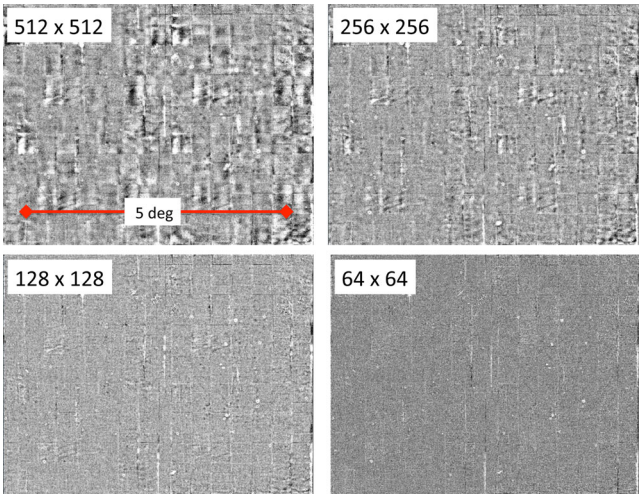

Figure 6. Examples of sections of VIKING data with various background subtractions as indicated.

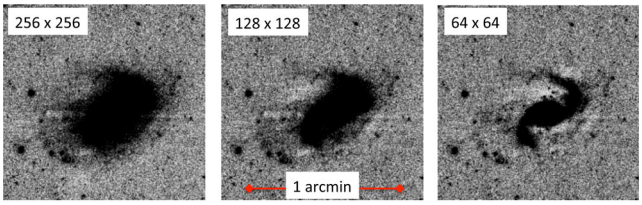

Figure 7. An illustration of the impact of oversmoothing the background on extended objects. The galaxy shown is the largest system in the GAMA region, NGC 0895 (located in G02). In the rightmost panel a significant portion of the galaxy has been removed due to the 64 × 64 pixel sky-subtraction process.

of the tiling becomes apparent in the SWarp (see Fig. 6), too low and galaxy photometry can be affected (see Fig. 7). To optimize the background filter size, we produced frames with a range of background filter sizes and performed structural analysis of the brightest 100 galaxies using SIGMA (Kelvin et al. 2012). Fig. 8 shows the magnitude offsets and Fig. 9 shows how the measured major-axis half-light radii vary with background mesh size. We tested pixel grids of 512 × 512, 256 × 256, 128 × 128, and 64 × 64 and only the smallest filter size had any noticeable impact on the measured properties and hence the second smallest filter size was adopted. Note that this finer filtering (compared to SDSS) is absolutely necessary because of (a) the mode of observation (pointed v drift-scan) and (b) the higher-degree of sky spatial variations in the near-IR wavebands.

2.4 *WISE*

The *WISE* (Wright et al. 2010) is a medium-class explorer mission operated by NASA and was launched on 2009 December 14. Following approximately one month of checks *WISE* completed a shallow survey of the entire sky in four IR bands (3.4, 4.6, 12, and 22 μm) over a 10 month period. *WISE* is built around a 40-cm telescope with a 47 arcmin × 47 arcmin field-of-view, and scans the sky with an effective exposure time of 11 s per frame. Each region of sky is typically scanned from tens to hundreds of times (with fields further from the ecliptic being observed more frequently). This allows the construction of deep stacked frames reaching a minimum 5σ point source sensitivity of 0.08, 0.11, 0.8, and 4 mJy in

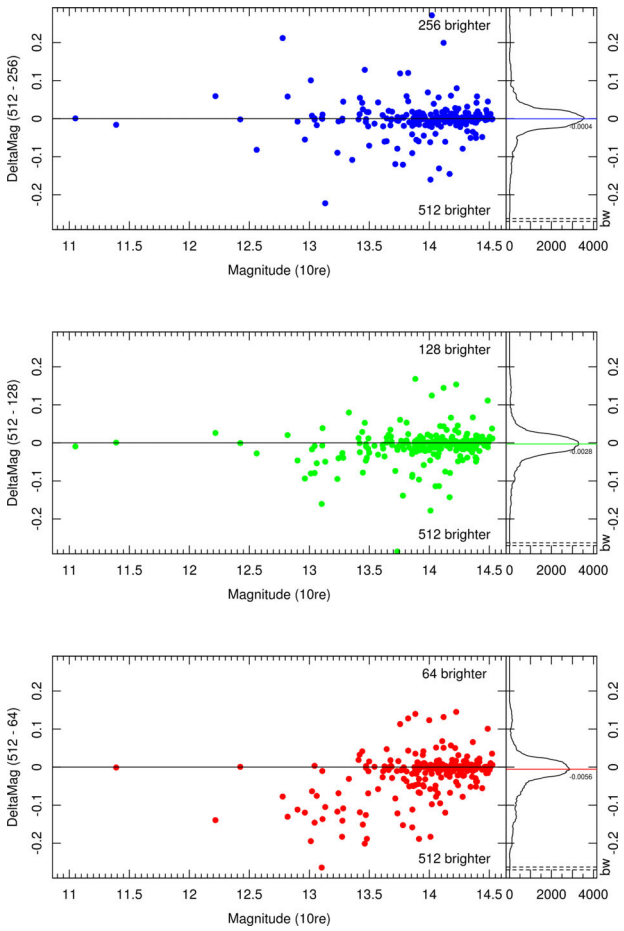

Figure 8. A comparison of flux measurements of the brightest 100 galaxies with varying background subtraction meshes. In each case the flux is compared against that derived from the 512 × 512 pixel background mesh. In general, it is only galaxies brighter than 14th magnitude with the 64 × 64 background mesh whose photometry is compromised.

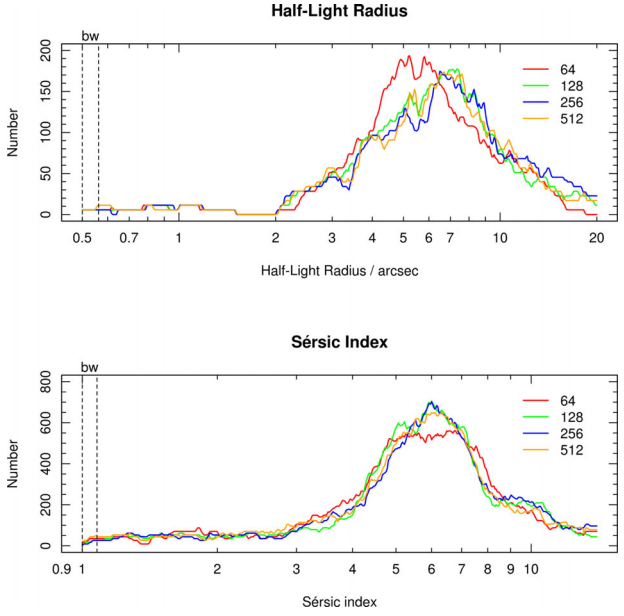

Figure 9. The major-axis half-light radius (upper panel) and the Sérsic index distributions (lower panel) for the brightest 100 galaxies for various background mesh sizes as indicated.

the *W*1(3.4 μm), *W*2(4.6 μm), *W*3(12 μm), and *W*4(22 μm) bands (see Wright et al. 2010). The base 'Atlas' data consist of direct stacks and associated source catalogues which are publicly available via the *WISE* and AllWISE data release hosted by the Infrared Science Archive (IRSA). These public data have PSF FWHM resolutions of ∼8.4, 9.2, 11.4, and 18.6 arcsec in *W*1, *W*2, *W*3, and *W*4, respectively, and a 1.375 arcsec pixel^{-1} scale. However, because of the stability of the PSF of the *WISE* system, higher resolution can be attained using deconvolution techniques, in particular 'drizzled' co-addition and the Maximum Correlation Method (MCM) of Masci & Fowler (2009; see Jarrett et al. 2012). Here, we use data which have been re-stacked via the drizzle method as the MCM or HiRes method is computationally expensive and only suited for very large nearby galaxies (see Jarrett et al. 2012, 2013). In brief this involves:

(1) gain-matching and rescaling the data ensuring a common photometric zero-point calibration,
(2) background level offset-matching,
(3) flagging and outlier rejection,
(4) co-addition using overlap area weighted interpolation and drizzle.

Here, drizzle refers to the variable pixel linear reconstruction technique of co-addition using a point response function kernel to construct the mosaics. Full details are provided in the *WISE* ICORE documentation (Masci 2013). The drizzled data result in final point-source FWHM of 5.9, 6.5, 7.0, and 12.4 arcsec (respectively), see Cluver et al. (2014) and Jarrett et al. (2012) for further details. Fig. 10 shows a comparison for one of our GAMA galaxies between the 'Atlas' and drizzled image in each of the four bands. The 'drizzled' frames are provided to the GAMA team stacked, calibrated to a common zero-point, and background subtracted in sections of 1.°56 × 1.°56. These frames are then SWarped into a single large mosaic at the native pixel resolution of 1 arcsec using the same field centre, and projection system as for the previous data sets. In re-gridding the data, we also include the SWARP background subtraction using a 256 × 256 pixel filter.

2.5 *Herschel*-ATLAS

The *Herschel* Space Observatory (Pilbratt et al. 2010) is operated by the European Space Agency (ESA) and was launched on 2009 May 14 and conducted a number of major survey campaigns during its 3.5 yr of operation. The largest extragalactic survey, in terms of areal coverage, is The *Herschel*-ATLAS (Eales et al. 2010). *Herschel*-ATLAS images were obtained using Herschel's fast-scan parallel mode and covered ∼600 deg^2 of sky in five distinct sky regions which included the four principal GAMA fields. The co-ordinated observations used both the PACS (Poglitsch et al. 2010) and SPIRE (Griffin et al. 2010) instruments to obtain scans at 100, 160, 250, 350, and 500 μm, i.e. sampling the warm and cold dust components of galaxies from $z = 0$ to 4. The final maps were the combination of two orthogonal cross-scans giving rise to PSFs with Gaussianized FWHM of 9.6 and 12.5 arcsec in 100 and 160 μm and 18, 25, and 35 arcsec in the 250, 350, and 500 μm bands, respectively (see Valiante et al. in preparation for full details of the PSF characterization). The data were processed, calibrated, nebularized to remove large-scale fluctuations due to cirrus and large-scale clustering of high-z sources, (see Valiante et al. in preparation; Maddox et al. in preparation), and finally mosaicked by the *Herschel*-ATLAS data reduction team who provided the final maps and 5σ source detection

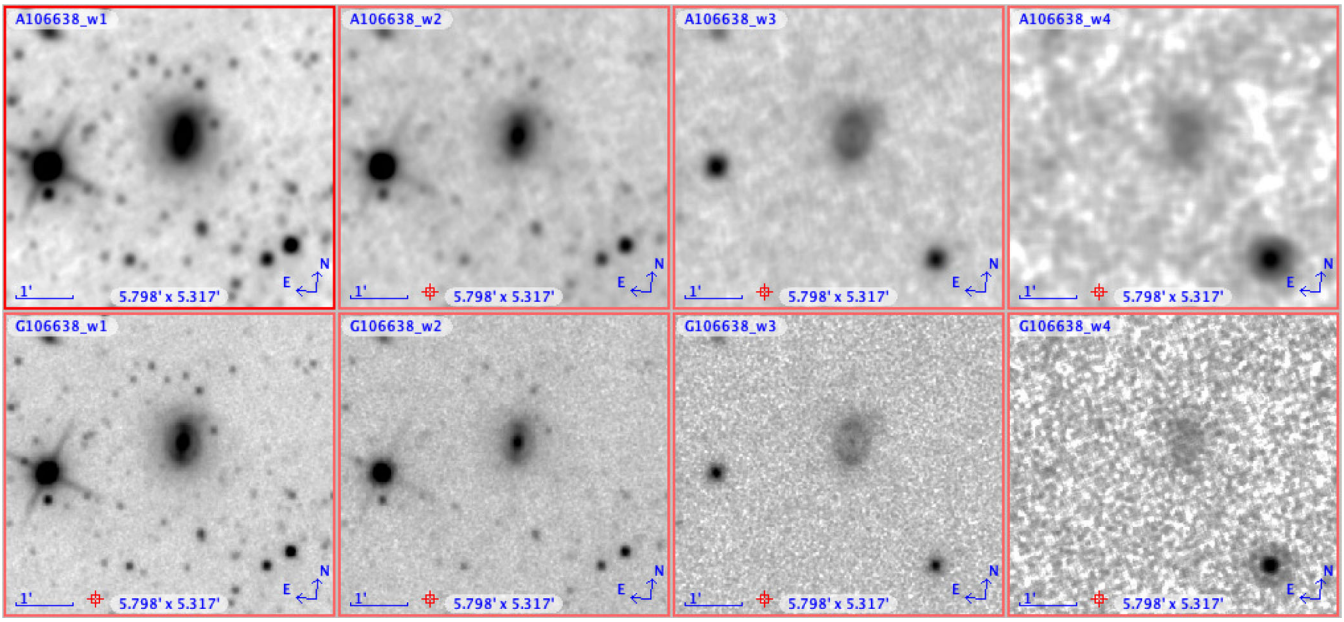

Figure 10. A visual comparison of *WISE* Atlas images (upper rows) and *WISE* drizzled images (lower rows) for bands *W*1, *W*2, *W*3, *W*4 (left-to-right). The panels are displayed over comparable ranges and the improvement in spatial resolution via the drizzling technique is self-evident. For details of the drizzling technique see Jarrett et al. (2011).

catalogues. The reduction process for the two instruments are described in detail in Ibar et al. (2010), and Pascale et al. (2011), to be superseded shortly by Valiante et al. (in preparation), and the method for source detection is described in detail in Rigby et al. (2011) also updated in Valiante et al. (in preparation). The absolute zero-point calibration is accurate to ±10 per cent for PACS and ±7 per cent for SPIRE which provides a potential systematic pedestal in addition to the random sky and object photon noise errors estimated later. Note that as the *Herschel*-ATLAS data have not yet been publicly released they remain subject to change. Every attempt will be made to ensure the online GAMA PDR provides notifications of any changes or updates.

To date the *Herschel*-ATLAS data have been used to study the dust and star formation properties of both near and distant galaxies based on far-IR/optical matched samples (see for example Dunne et al. 2011; Smith et al. 2011, 2012; Bourne et al. 2012; Rowlands et al. 2012). To pre-prepare the data for GAMA, we re-SWarp the mosaics provided on to a uniform grid using the field centres from Table 1 using the TAN WCS projection, and preserving the original pixel size as specified in the file headers and shown on Table 2.

2.6 Cosmetic and noise characteristics of the GAMA SWarp set

To assess the quality of GAMA SWarps, we derive the background noise distributions (i.e. sky-subtracted), within selected regions for each of our LOW-RES (i.e. 3.39 arcsec) SWarps, which are displayed from -2σ to $+2\sigma$ in Figs A1–A4 for G09, G12, G15, and G23, respectively. The black rectangle represents the GAMA region and the dotted blue rectangle the selected region from which the noise characteristics are derived (the mode and 3σ-clipped standard deviation). These images show no obvious major sky gradients across the sky regions, however, they do show interesting substructure which highlights correlations in the underlying noise properties. In most cases the correlations highlight the genesis, i.e. the SDSS stripes, *GALEX* pointings, and VIKING PAW-PRINTS. In these cases, the noise properties for each particular frame/scan is dictated by the conditions during observations (SDSS and VISTA) or the variability of the various integration times (*GALEX*). While uniform backgrounds are highly desirable, these are never achieved in practice. Some SDSS scans will be slightly less noisy than others and some PAW-PRINTS will have significantly amplified noise characteristics. Interestingly, the *WISE* and *Herschel*-ATLAS data show the least structure which mainly reflects the benefits of using fixed integration times as well as operating outside the confines of a time-varying atmosphere. However, some impact of observing close to the moon is apparent in the *WISE* G12 SWarps. Also noticeable in the *Herschel*-ATLAS data is the reduced noise in the overlap regions as expected.

The noise distributions derived from the GAMA SWarps are shown in Table 3, for *GALEX*, SDSS, VISTA, and *WISE* data these statistics are derived from fitting a Gaussian distribution to the histogram of data values below the mode. They therefore do not include any confusion estimate and assume the noise is uncorrelated. In all cases, the distributions are very well described by a normal distribution implying that the systematic frame-pistoning (i.e. ZP offsets) in the data (arising from the independent calibration of the distinct pointings), is operating at a relatively low level and within the range of the pixel-to-pixel variations. Using the 3σ-clipped standard deviations we derive (analytically) the 1σ surface brightness limits and the 5σ point-source detection limits for each of the SWarp images (see Table 3). For the PACS and SPIRE data, where correlated noise is believed to be an issue, we derive the 5σ detection limits directly by placing apertures equivalent to the beam size at random locations across the SWarps and measuring the standard deviation of the resulting aperture fluxes (again fitting to the distribution below the mode). In Fig. 11, the GAMA SWarp detection limits are compared to the values listed online for each facility (as indicated by the colour lines). For *GALEX* MIS, SDSS DR7, and VIKING,

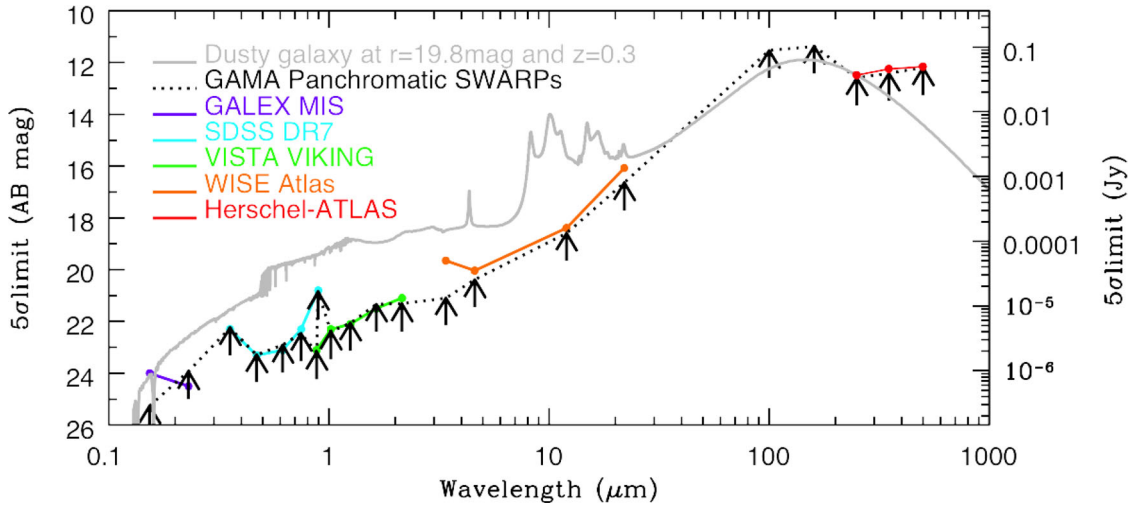

Figure 11. The sensitivity reached in each band as derived from the GAMA SWarps (black lines) and compared to the listed values (coloured lines). Also shown in grey is a typical SED for a dusty galaxy with $r_{AB} = 19.8$ mag.

the depths probed agree extremely well. Note that our derived *WISE* *W*1 band limit appears significantly deeper than that quoted by the *WISE* collaboration this is because our values ignore confusion (i.e. fits to the negative noise distribution), whereas the *WISE* quoted value incorporates this aspect. For *Herschel*-ATLAS SPIRE, we note that the agreement with the SPIRE values reported in Valiante et al. (in preparation) is extremely good.

2.7 Astrometric verification

To check the astrometric alignment of the SWarps we run SExtractor over either the entire SWarp set (*GALEX*, *WISE*, and *Herschel*) or a 4 deg^2 section from G12 (SDSS and VIKING, to keep CPU requirement manageable). We use relatively high signal-to-noise cuts of 100 (*GALEX*, where the data is not uniform), 10 (*WISE* and *Herschel*), or 3 (SDSS and VIKING). We then match to either the GAMA InputCat with $r < 17.0$ mag (*GALEX*, SDSS, VIKING, and *WISE*) or the GAMA TilingCatv45 with $r < 17.0$ mag and $(u - g) < 1.5$ (*Herschel*-ATLAS) to isolate star-forming galaxies. Fig. 12 shows the resulting Δ RA and Δ Dec diagrams for each band compared to the canonical *r*-band data (grey data points). In Fig. 12, the blue cross (mostly not visible) defines the centroid and the thick green circle indicates the PSF FWHM for that band. The thick blue band defines the region which encloses 66 per cent of the population (after accounting for the density of random mismatches), and the thin blue circles enclose either 50 or 80 per cent of valid matches. Fig. 12 highlights that in all cases the centroid of the RA and Dec offset is extremely close to zero (below 0.3 arcsec in all bands with the FUV and NUV showing the largest offsets, and below 0.02 arcsec in the optical and near-IR), and that the 66 per cent sprawl lies within 0.5 $\times$ the PSF FWHM in all bands. We therefore consider the astrometry to be as one would expect given the respective FWHM seeing values.

2.8 Visual inspection of the combined data and data access

Our full data set is diverse and the volume large. In order to inspect the data, we have developed a publicly available online tool which provides both download links to the individual SWarps, as well as an option to extract image regions from the data set. Users can also build RGB colour images using any of the 21 bands as well as overlay contours and basic catalogue information (e.g. GAMA IDs, photometry apertures, and object locations). The GAMA Panchromatic SWarp Imager (Ψ) is therefore extremely versatile and useful for exploring the data volume: http://gama-psi.icrar.org/. Figs 13–15 show examples of various extractions using the tool with Fig. 13 showing the significant increase in depth from the SDSS *z*-band data to the VISTA VIKING *Z* band. Fig. 14 shows a single GAMA galaxy in 20 of the 21 bands (note that the SDSS *z* band is not shown here), and Fig. 15 shows various colour combinations with contours, IDs and apertures overlaid as indicated. Note that searches can be made based on GAMA ID *or* RA and Dec and is therefore of use to high-*z* teams with objects in the GAMA regions (e.g. *Herschel*-ATLAS team).

Using GAMA Ψ via the link above, one can also access the individual SWarps files including the native, convolved and weight-maps and the XML files which contain, the pixel data, a description of the weights, and a listing of the constituent files making up the SWarp, respectively. The weight-maps are particularly useful and can be used to determine both the coverage and provide a mask. Zero values in the weight SWarp imply no data, while non-zero values imply coverage. These weight-maps have been used to generate the coverage statistics shown in col. 7 of Table. 3. The SWarps, weight-maps, and XML files can all be downloaded from: http://gama-psi.icrar.org/panchromaticDR.php. However, note that files sizes vary from 100 KB (for XML files) to up to 80 GB (for SWarps and weight-maps).

3 PANCHROMATIC PHOTOMETRY FOR G09, G12, AND G15 ONLY

Vital to successful analysis of panchromatic data are robust flux measurements, robust errors, and a common deblending solution. This is particularly difficult when the flux sensitivities and spatial resolutions vary significantly, as is the case with the GAMA PDR (see Figs 11, 14, and 15, i.e. 35 to 0.7 arcsec spatial resolution). In an ideal situation one would define an aperture in a single band and then place the same aperture at the same astrometric location in data with identical spatial sampling. This is the strategy we pursued in Hill et al. (2011, see also Driver et al. 2011) to derive $u - K_s$

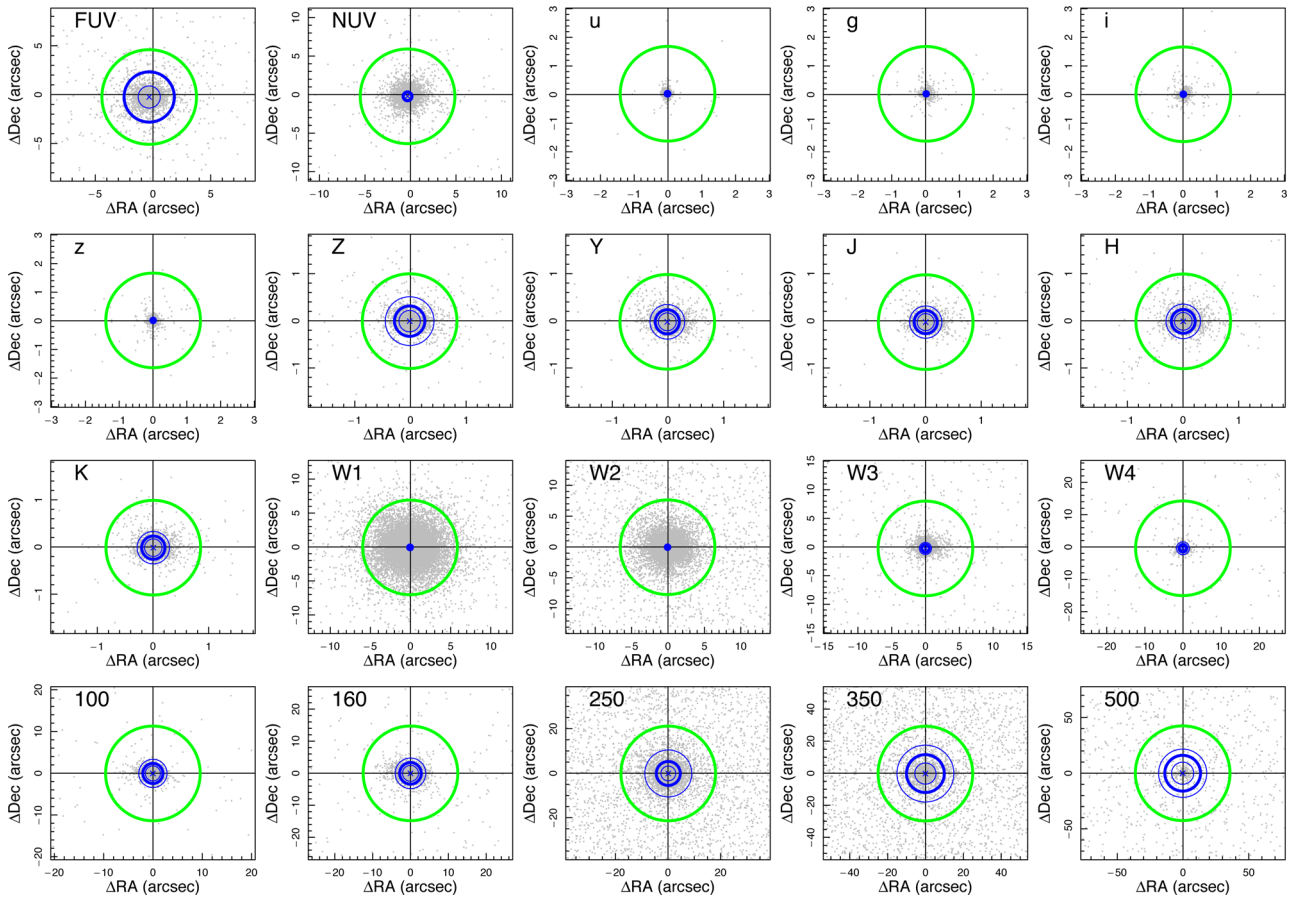

Figure 12. Confirmation of the astrometric accuracy. Each diagram shows the positional offsets of that particular band against the *r*-band GAMA Input or Tiling catalogues (grey data points). The centroid of the population is shown with a blue cross and the (native) PSF FWHM is shown as a green circle. The circles enclosing 50, 66, and 80 per cent of the population is shown by a thin, thick, and thin blue line, respectively. In all cases the relative astrometry is robust to <0.1PSF FWHM, and the 66 per cent spread enclosed with 0.5× the PSF FWHM.

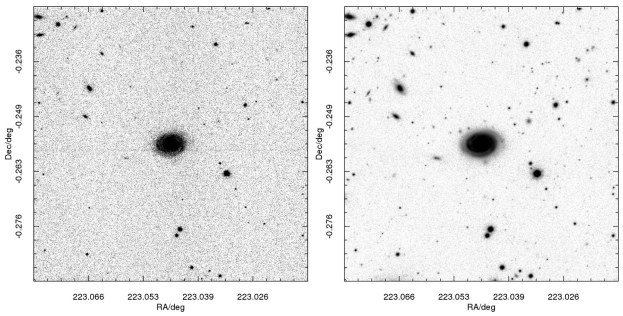

Figure 13. A comparison of the quality of the SDSS *z*-band data (left) against the VISTA VIKING *Z* band (right).

aperture-matched photometry (using the seeing-convolved SWarps convolved to a 2 arcsec FWHM). While we can still implement this strategy in the *u* to K_s range (see Section 4.2 below), we cannot easily extend it outside this wavelength range because of the *severe* resolution mismatch (see Table 2). Software (LAMBDAR) is being developed to specifically address this issues and will be described in a companion paper (Wright et al. in preparation). In the meantime, we assemble a benchmark panchromatic catalogue from a combination of aperture-matched photometry, table matching, and optically motivated (forced) photometry. It is worth noting that the GAMA PDR assembled here while heterogeneous across facilities is essentially optimized for each facility, and therefore optimal for studies not requiring broad panchromatic coverage.

In the FUV and NUV, we use the GAMA *GALEX* catalogue described in Liske et al. (2015) and which uses a variety of photometry measures including curve-of-growth and the *GALEX* pipeline fluxes. In the optical and near-IR, we apply the aperture-matched method mentioned above and described in detail in the next sections. In the mid-IR we use the *WISE* catalogues described in Cluver et al. (2014). Longwards of the *WISE* bands, we adopt a strategy developed by the *Herschel*-ATLAS team (Bourne et al. 2012, see Appendix A) to produce optically motivated aperture measurements (sometimes referred to as forced photometry). This is applied to all GAMA targets which lie within the PACS and SPIRE 100 to 500 μm data.

3.1 Aperture-matched photometry from *u* to K_s: IOTA

The *u* to K_s band data have been convolved to a common 2 arcsec FWHM seeing (see Fig. 3). For each object in the GAMA tiling catalogue with a secure redshift (TilingCatv44, i.e. a valid galaxy target within the specified regions with $r_{\rm AB} < 19.8$ mag, see Baldry et al. 2010) we perform the following tasks:

(1) extract a 1001 × 1001 pixel region in all 10 bands (*ugrizZYJHK*$_s$),

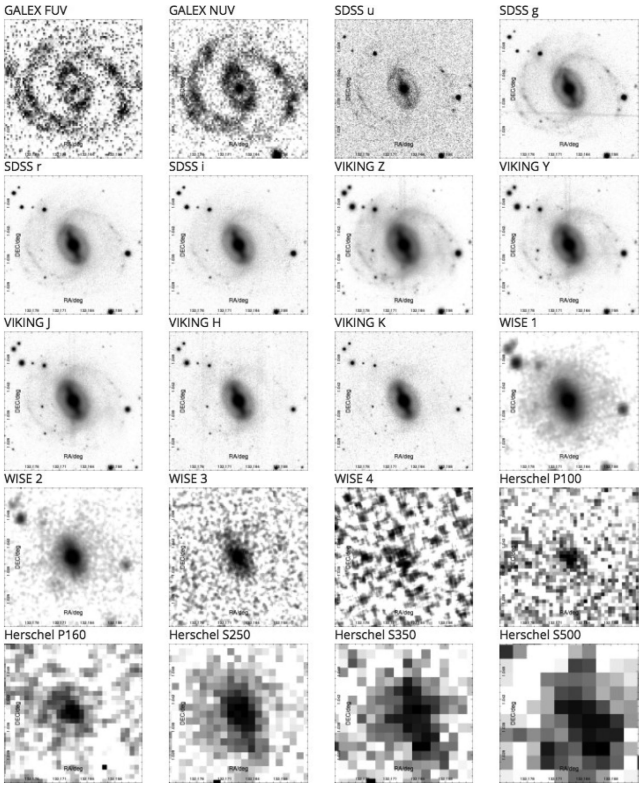

Figure 14. 20 band panchromatic imaging for a 1 arcmin × 1 arcmin region centred on GAMA galaxy G371633. Filters increase in wavelength proceeding from left to right and top to bottom, note the SDSS z filter is omitted, i.e. FUV, NUV, u, g, r, i, Z, Y, J, H, K, $W1$, $W2$, $W3$, $W4$, 100, 160, 250, 350, 500. Produced using the GAMA Ψ: http://gama-psi.icrar.org/.

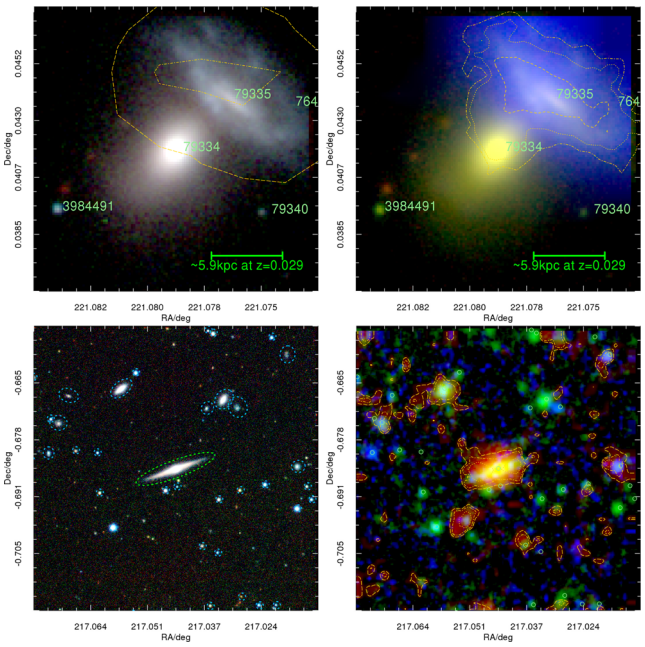

Figure 15. Upper left: a colour composite image of G79334 produced by combining the SDSS g and r with the VIKING H band images. Overlaid are the contours from SPIRE-250 band. GAMA IDs are marked. Upper right: a colour composite of G79334 from *GALEX* NUV, VIKING Z and K_s and with contours overlaid from *WISE*. Lower left: a 2 arcmin × 2 arcmin colour composite centred on G48432 made from data extracted from the GAMA SDSS r and i SWarp combined with the VIKING H SWarp and with the apertures used for the aperture-matched photometry overlaid (lower right). A composite colour image of G48432 made from *GALEX* FUV (blue channel), *WISE* $W1$ (green channel) and SPIRE 250 μm (red channel and contours). All images produced using the online GAMA Ψ tool: http://gama-psi.icrar.org/.

(2) run SExtractor in dual object mode with r as the primary band,

(3) identify the SExtractor object closest to the central pixel (2 arcsec max),

(4) extract the photometry for this object in the two bands,

(5) repeat for all bands.

In essence this process relies on SDSS DR7 for the initial source detection and initial classification including an r-band Petrosian flux limit to define the input catalogue. However, the final deblending and photometry is ultimately based on SExtractor (using the parameters described in Liske et al. 2015 optimized for our convolved data). An identical aperture and mask and deblend solution – initially defined in the r band – is then applied to the $ugizZYJHK_s$ bands. In order to manage this process efficiently for 220k objects we use an in-house software wrapper, IOTA.

3.2 Recalibration of the u to K_s photometry

The VIKING data are relatively new and to assess the absolute zero-point errors, we test the consistency of the photometry between our measured VIKING data and the 2MASS point source catalogue. We achieve this by extracting all catalogued stars in the extended GAMA regions from InputCatv06 which itself is derived from SDSS DR7 (see Baldry et al. 2010). To obtain near-IR flux measurements we uploaded the objects classified as stars (see Baldry et al. 2010) to the IPAC IRSA and queried the 2MASS All-Sky Point Source Catalogue (on 2013-06-07). We obtained 498 637 matches for which photometry existed in one or more of the 2MASS bands (JHK_s). This sample was trimmed to the exact GAMA RA extents to produce catalogues of 201 671, 92 224, and 131 976 stars in G09, G12, and G15, respectively. We ran IOTA on these objects to derive $ugrizZYJHK_s$ photometry based on Kron apertures with a minimum aperture diameter of 5 arcsec. Figs 16 and 17 show the resulting zero-point comparisons versus magnitude (left-hand panels) and versus the VIKING $(J-K)_{\rm AB}$ colour (right-hand panels) for filters $ugrizZJHK_s$ (top to bottom), respectively. Note that for the $ugriz$ bands, we compare directly to SDSS PSF magnitudes corrected to AB (i.e. $u_{\rm AB} = u_{\rm SDSS} - 0.04$ and $z_{\rm AB} = z_{\rm SDSS} + 0.02$) for the $ZJHK_s$ bands we convert the 2MASS magnitudes into the VISTA passband system, using the colour transformations derived by the VISTA Variables in the Via Lactea Survey (VVV) team (Soto et al. 2013) which are

$$J_{\rm VISTA} = J_{\rm 2MASS} - 0.077(J_{\rm 2MASS} - H_{\rm 2MASS}), \quad (2)$$

$$H_{\rm VISTA} = H_{\rm 2MASS} + 0.032(J_{\rm 2MASS} - H_{\rm 2MASS}), \quad (3)$$

$$K_{\rm VISTA} = K_{\rm 2MASS} + 0.010(J_{\rm 2MASS} - K_{\rm 2MASS}). \quad (4)$$

Finally, we implement the Vega to AB correction appropriate for the VISTA filters, see Table 2.

At brighter magnitudes the deeper VIKING data will suffer from saturation, and at fainter magnitudes the shallow 2MASS data

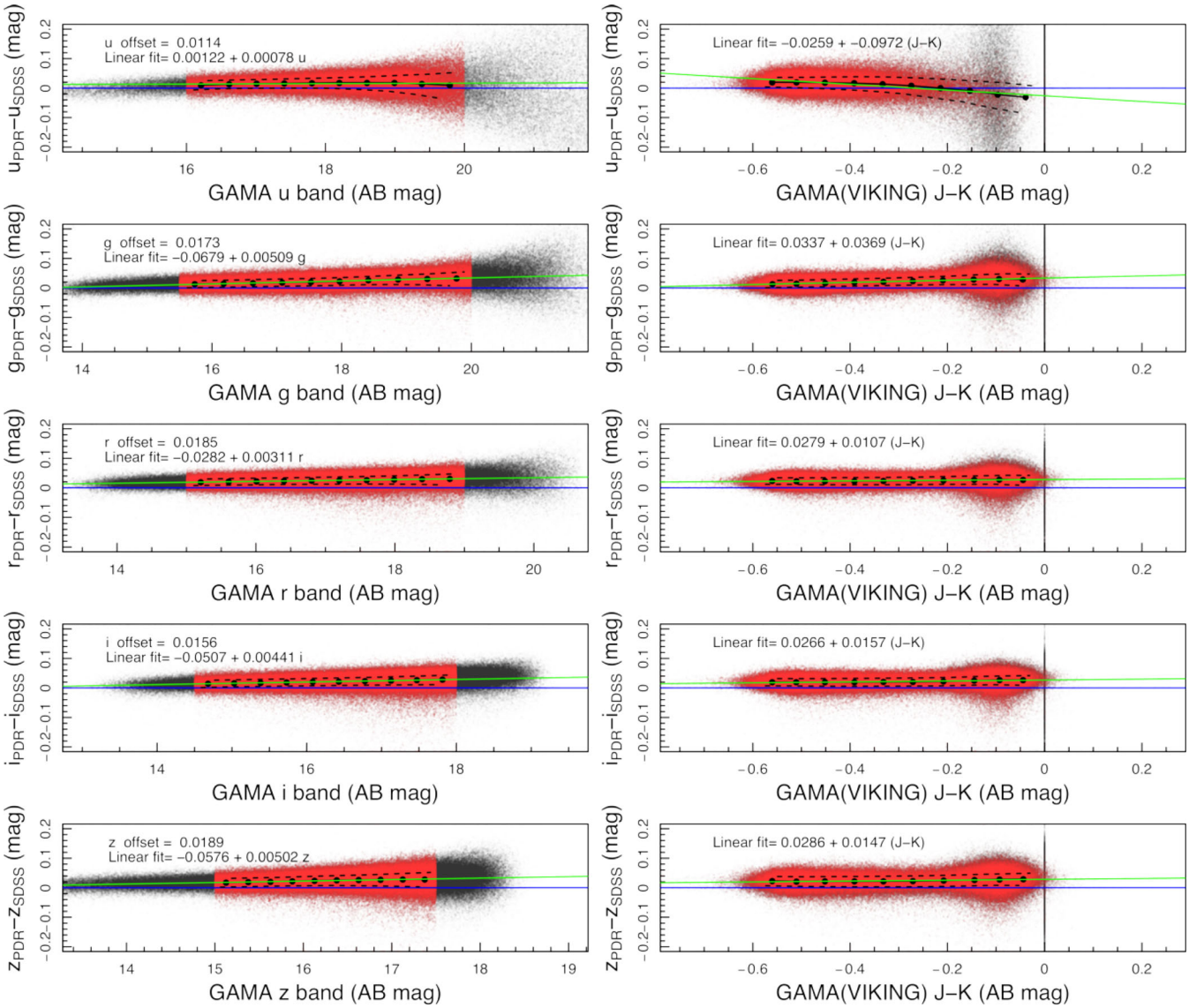

Figure 16. Comparison between SDSS PSF photometry versus SDSS (IOTA) for 420k stars. Highlighted in red are data deemed to lie in the flux and colour regions for which comparisons can be made.

will become swamped by noise. Figs 16 and 17 show the direct comparisons (black data points), and the data which we consider robust to saturation and limiting signal-to-noise (red data points). Also shown in the figures are the derived global offset values (blue lines), and the simple linear fits (green lines) to the medians (black squares with error bars) for both the magnitude (left) and colour comparisons (right). The dotted lines indicate the quartiles of the data.

We conclude that the absolute zero-point calibration is robust across the board to ±0.02 mag within the magnitude and colour ranges indicated (red data points). However, it is extremely important to recognize that the majority of our galaxies lie significantly outside the flux and colour ranges which we are examining here. As we shall discuss in Section 3.4 this can cause significant and intractable issues. To quantify the potential for zero-point drift between the calibration regime and operating regime we show in Table 4 possible zero-point offsets one might derive at the typical flux and the typical colour of the GAMA sample using either (a) a simple offset (Figs 16 and 17 blue line), (b) a linear fit with magnitude (the linear fit shown as a green line in Figs 16 and 17, left-hand panels) and, (c) a linear fit with colour (the linear fit shown as a green line on Figs 16 and 17, right-hand panels). Any one of these relations, or some combination of, could be valid and hence the range reflects the uncertainty in the absolute zero-point calculations for our filters. We elect not to correct our data using any of these zero-points but instead incorporate the possible systematic zero-point error (indicated in the final column) into our analysis.

3.3 $u - K_s$ photometry errors

Critical to any SED fitting algorithm will be the derivation of robust errors for each of our galaxies in each band. Here, we derive the errors from consideration of: the zero-point error ($\sigma_{\rm ZP}$), the random sky error ($\sigma_{\rm SkyRan}$), the systematic sky error ($\sigma_{\rm SkySys}$), and the object

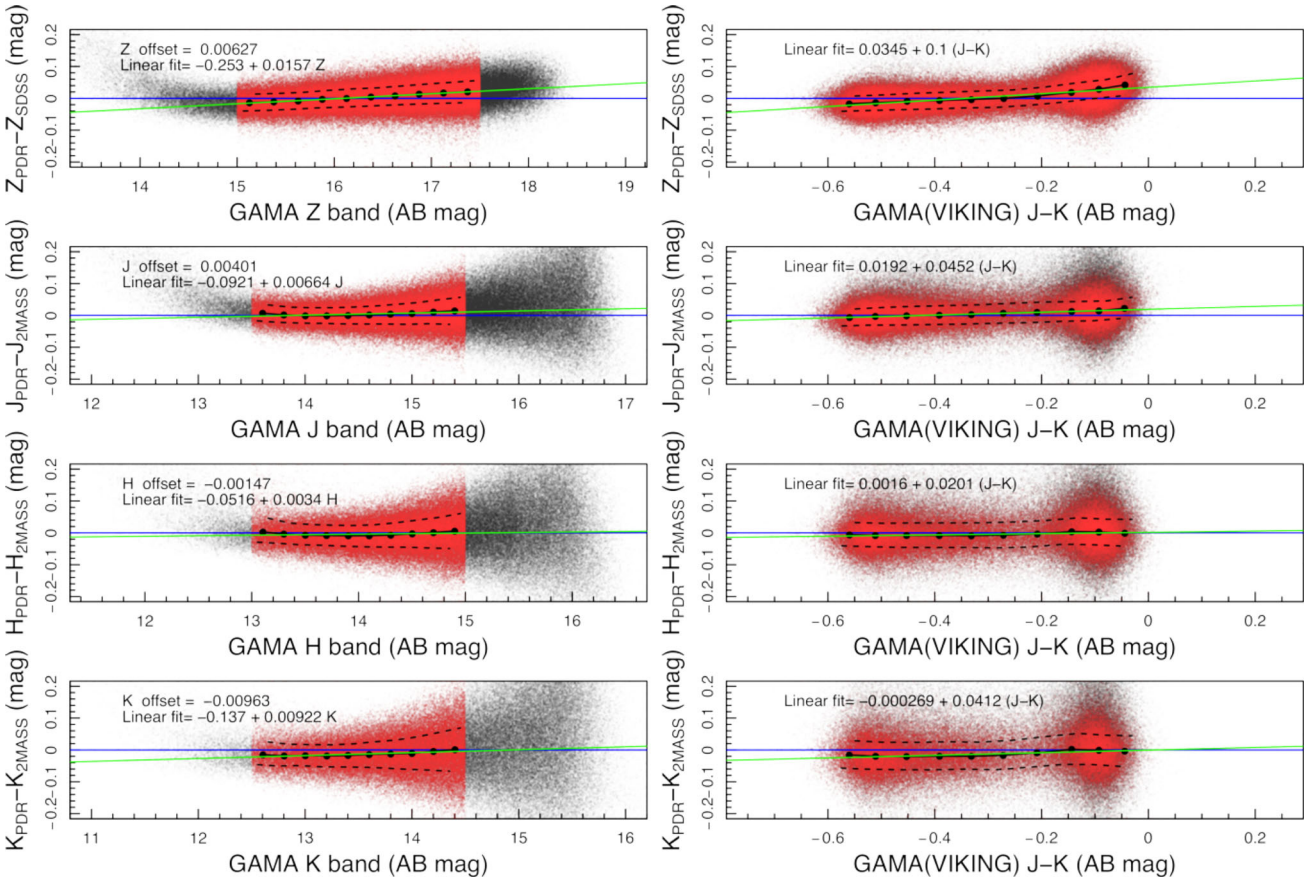

Figure 17. Comparison between 2MASS stellar photometry versus VIKING (IOTA) for 420k stars. Highlighted in red are data deemed to lie in the flux and colour regions for which comparisons can be made.

Table 4. Zero-point uncertainties in each band.

Band	GAMA Median flux limit (mag)	GAMA Median $(J-K_s)$ colour (mag)	Potential zero-point (ZP) offsets Absolute	linear with mag.	linear with colour	ZP unc. Mean ± Std.	Adopted ZP error
u	21.48	0.37	+0.011	+0.018	−0.020	+0.003 ± 0.020	0.02
g	20.30	0.40	+0.017	+0.035	+0.048	+0.033 ± 0.016	0.05
r	19.35	0.41	+0.018	+0.032	+0.032	+0.027 ± 0.008	0.03
i	18.88	0.41	+0.016	+0.033	+0.033	+0.027 ± 0.008	0.03
z	18.60	0.41	+0.019	+0.036	+0.035	+0.030 ± 0.008	0.03
Z	18.61	0.41	+0.006	+0.039	+0.076	+0.040 ± 0.035	0.08
Y	18.38	0.42	NA	NA	NA	NA	0.10
J	18.16	0.43	+0.004	+0.028	+0.037	+0.023 ± 0.017	0.04
H	17.84	0.44	−0.015	−0.050	+0.010	−0.018 ± 0.030	0.05
K	17.69	0.44	−0.010	+0.026	+0.018	+0.011 ± 0.019	0.03

shot noise ($\sigma_{\rm Shot}$). The first of these is quoted in Table 4, the other three can be given by

$$\sigma_{\rm SkyRan} = \sqrt{N_{\rm Pix}}\sigma_{\rm Sky} \quad (5)$$

$$\sigma_{\rm SkySys} = N_{\rm Pix}\frac{\sigma_{\rm Sky}}{\sqrt{N_{\rm Aper}}} \quad (6)$$

$$\sigma_{\rm Shot} = \sqrt{\frac{I_{\rm Obj}}{\gamma}}, \quad (7)$$

where $\sigma_{\rm Sky}$ is the sky noise give in Table 3 (col. 4), $N_{\rm Pix}$ is the number of pixels in the object aperture (given by $\pi R^2_{\rm KRON} A_{\rm IMAGE} B_{\rm IMAGE}$ in terms of Source Extractor output parameters), and $N_{\rm Aper}$ is the number of pixels used in the aperture in which the local background was measured (i.e. $\pi R^2_{\rm KRON}(A_{\rm IMAGE}+32)(B_{\rm IMAGE}+32) - N_{\rm pix}$) and γ is the gain. Of these only the gain is uncertain as during the stacking and renormalizing of the data the gain is modified from its original value by varying amounts (see for example the distribution of multipliers in Fig. 5). However, as the vast majority of our galaxies are relatively low signal-to-noise detections the sky errors swamp the object shot noise errors and hence we elect to omit the object shot noise component in our final error analysis.

3.4 Comparison to earlier GAMA photometry

Finally, we compare our revised SDSS+VIKING photometry to our earlier SDSS+UKIDSS photometry in Fig. 18. In this

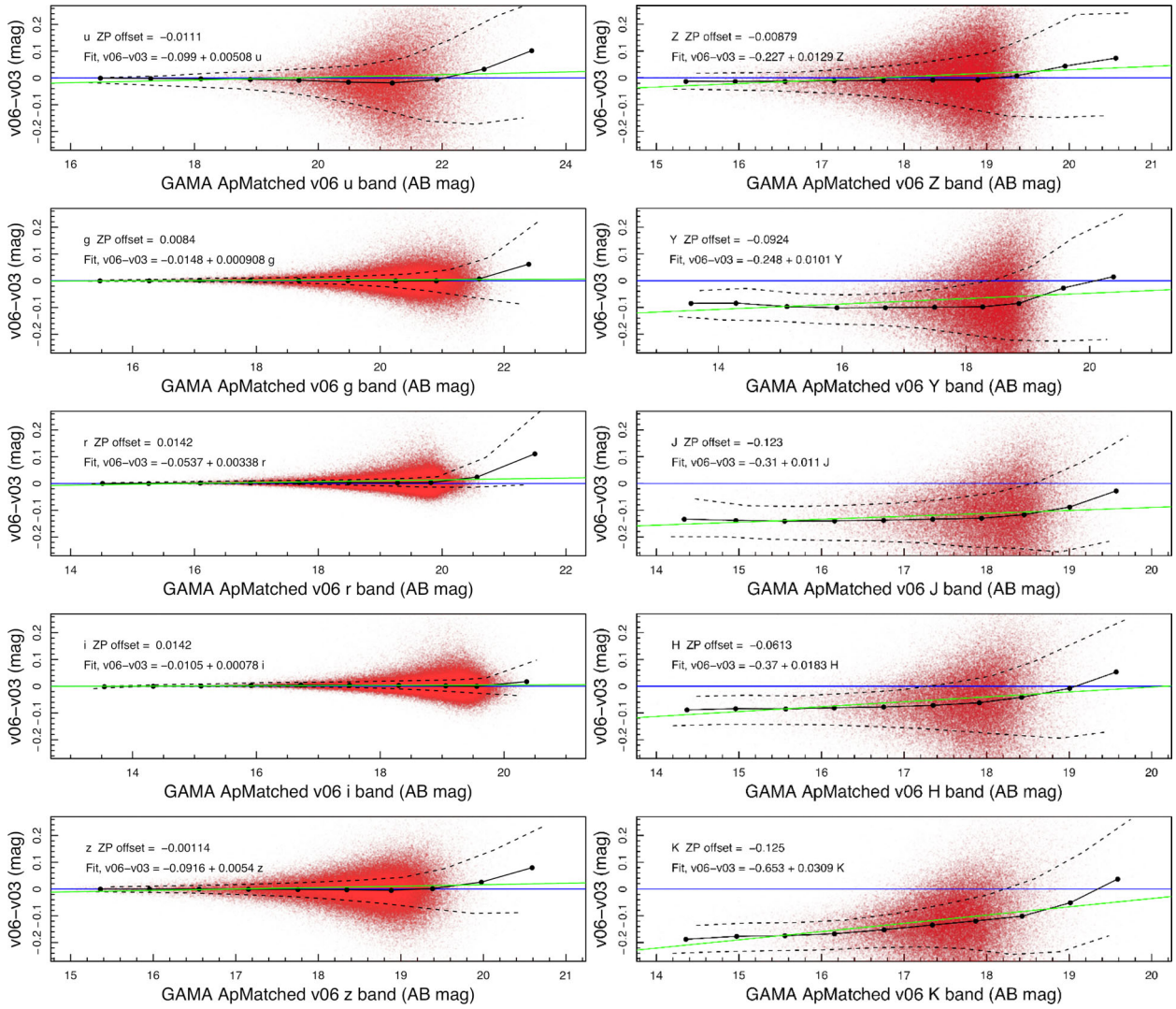

Figure 18. Comparison between GAMA ApMatchedv03 and GAMA ApMatchedv06 (i.e. PDR) *ugrizZYJHK*$_s$ galaxy photometry. Filter transformations as indicated in the text.

implementation of IOTA the only difference in the *ugriz* bands is the move from a global background estimation (fixed value across the background subtracted frame) to a local background estimation. The impact appears minimal with zero-point offsets less than ±0.015. However in the *YJHK*$_s$ bands, we notice significant offsets between the UKIDSS and VIKING flux measurements. The reasons for this are subtle and while they have not been exhaustively pursued we believe are most likely due a hidden linearity issue in the UKIDSS pipeline. In Fig. 19, we show our flux measurements from our UKIDSS data for 420k SDSS selected stars for which we have 2MASS photometry. The agreement is once again good, however in all cases there are significant gradients in the data and significantly stronger than those we saw in the VIKING data (refer to Fig. 17). Extrapolating the linear fits to the flux and colour regions where the majority of our galaxies lie we infer the level of offsets seen in Fig. 18. The implication is that there *may* be a linearity issue with the UKIDSS calibration. Note that as Hill et al. (2010) have shown our in-house UKIDSS photometry agrees extremely well with that provided from the UKIDSS archive. We do not explore this issue further but, as a number of earlier GAMA papers are based on UKIDSS photometry, we include the UKIDSS SWarps in the public release, while cautioning against their use.

3.5 Optical motivated far-IR photometry

To derive our far-IR photometry for every GAMA target, we implement an optically motivated approach (also referred to as forced-photometry). This technique closely follows the approach developed by Bourne et al. (2012) for the *Herschel*-ATLAS team and which has been used to obtain SPIRE photometry at the location of known optical sources. The method adopts as its starting point the *r*-band apertures determined from our optically motivated source finding described earlier and uses the following parameter set for the apertures: right ascension, declination, major axis, minor axis, and position angle. For each far-IR band, the aperture defined by these parameters is combined with the appropriate PSF for each of the five bands (supplied by the *Herschel*-ATLAS team). The resulting 2D distribution therefore consists of a flat pedestal (within the originally defined aperture region) with edges which decline as if from the peak of the normal PSF. This soft-edge aperture can be imagined as a 2D *mesa*-like distribution function which can now be convolved with the data at the appropriate astrometric location. In the event of two *mesas* overlapping the flux is shared according to the ratio of the respective *mesa* functions at that pixel location, i.e. the flux is distributed using PSF and aperture information only

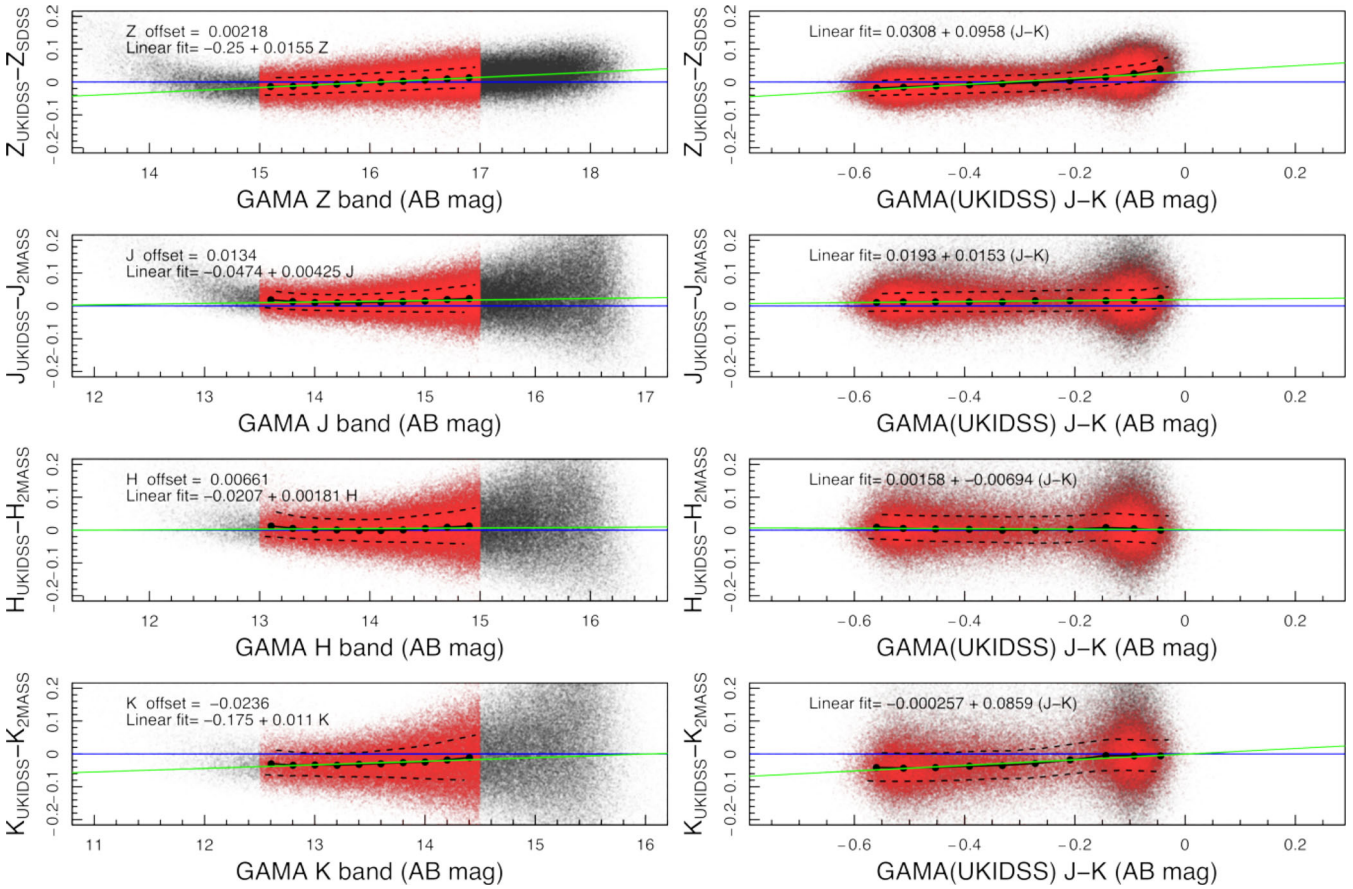

Figure 19. Comparison between 2MASS stellar photometry versus UKIDSS (IOTA) for 420k stars.

Table 5. Sky background levels per pixel as derived from blank apertures.

	Sky background (Jy)		
Band	G09	G12	G15
100 μm	0.000 2669	0.000 1491	0.000 2739
160 μm	0.000 2044	0.000 2436	0.000 3784

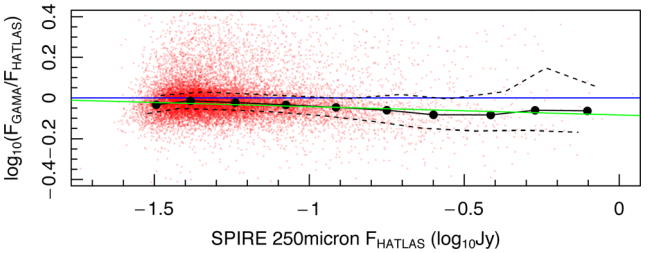

Figure 20. A comparison between the preliminary *Herschel*-ATLAS 5σ catalogue and the optically motivated catalogue derived here in the SPIRE 250 μm band. It should be noted that the zero-points calibration and entire reduction process have evolved between these catalogues. Note units are in Jansky as is standard in the far-IR.

and ignoring the intensity of the central pixel. Enhancements of this methodology are under development (Wright et al., in preparation) and will include consideration of the central peak intensity along with the inclusion of interlopers (i.e. high-z targets), and iterations. The recovered fluxes at this moment contain flux from the object, plus from any low-level contaminating background objects. To assess the level of contamination we made measurements in ∼30 000 apertures of comparable sizes to our object distribution which were allocated to regions where no known 5σ *Herschel*-ATLAS detection exists nor any GAMA object. The mean background level in these regions was found to be zero in all SPIRE bands, as expected since the maps are made to have zero mean flux and residual large-scale emission has been removed via the nebulizer step. In the PACS data small background values were found as shown in Table 5. To correct for this effect, the final step is to subtract the background values for the PACS data using the *effective* aperture pixel number and factoring in shared pixels where apertures overlap.

Fig. 20 compares our aperture-matched photometry against the *Herschel*-ATLAS 5σ catalogue produced by Smith et al. (2012). In general, the data agree reasonably well with offsets at the levels of 0.05 dex (12 per cent).

There have been changes in the PACS calibration and map-making algorithms between the generation of the values in Smith et al. (2012), Rigby et al. (2011) catalogues, and this work, and these changes have been substantial. Offsets at this level are consistent with these changes. For the SPIRE data, there have been no significant changes to the calibration or map-making process, however there are a number of potential issues with both the catalogues being compared in Fig. 20. First, the H-ATLAS catalogue is with a preliminary version of the H-ATLAS release catalogue (Valiante et al., in preparation) which does not include aperture photometry for resolved sources, explaining some of the scatter at the bright

end. Secondly, the largest optical sources, which correspond to the brightest H-ATLAS sources are often shredded by SExtractor which leads to inappropriately small apertures being used for the forced photometry, and this may lead to the offset between the catalogues at the bright end and contribute to the scatter.

In Wright et al. (in preparation), we will compare our updated LAMBDAR photometry with the final released version of the H-ATLAS catalogue (Valiante et al. in preparation) when all fluxes will be drawn from the same data pipelines and images.

3.6 Table matching the UV, optical/near-IR, mid-IR, and far-IR catalogues

At this stage we have a number of distinct catalogues.

GalexMainv02. This contains measurements of the FUV and NUV fluxes which have been assembled through the use of *r*-band priors combined with curve-of-growth analysis and is described in Liske et al. (2015). We adopt the BEST photometry values. In brief the BEST photometry is that returned by the curve-of-growth method with automatic edge-detection when the NUV semimajor axis is greater than 20 arcsec or when the GAMA object does not have an unambiguous counterpart. In other cases the BEST photometry is that derived from the standard pipeline matched to the GAMA target catalogue.

ApMatchedCatv06. This contains the *u*- to K_s-band photometry as described in detail in Section 3.1

WISEPhotometryv02. As described in Cluver et al. (2014) which outlines the detailed construction of the *WISE* photometry with two exceptions. First, for GAMA galaxies not resolved by *WISE*, standard aperture photometry (as provided by the AllWISE Data Release) is used instead of the profile-fit photometry (wpro). This is due to the sensitivity of *WISE* when observing extended, but unresolved sources, resulting in loss of flux in wpro values compared to standard aperture values (see Cluver et al., in preparation). Secondly, the photometry has been updated to reflect the AllWISE catalogue values. Note that this version of the catalogue also includes the correction to the updated *W*4 filter described in Brown et al. (2014a).

HAtlasPhotomCatv01. This contains the far-IR measurements as described in Section 3.5 based on optically motivated aperture-matched measurements incorporating contamination corrections.

We use TOPCAT to combine these catalogues by matching on GAMA CATAIDS (i.e. exact name matching), the FUV to K_s-band data are then corrected for Galactic extinction using the $E(B-V)$ values provided by Schlegel, Finkbeiner & Davis (1998; GalacticExtinctionv02) and the coefficients listed in Liske et al. (2015).

The combined catalogue is then converted from a mixture of AB magnitudes and Janskys to Janskys throughout, with dummy values included when the object has not been surveyed in that particular band. Coverage maps may be recovered from the catalogue using the dummy values alone.

4 ROBUSTNESS CHECKS OF THE PDR

As the GAMA PDR is constructed from a variety of distinct catalogues and pathways it is important to assess its robustness, accuracy, and outlier rate. In earlier figures (Figs 16–19), we showed direct comparisons of the magnitude difference between two data sets. These are good for identifying zero-point (i.e. systematic) offsets, but not particularly useful in establishing which of the two data sets is the more robust. Here we examine the more informative 'colour'-plots. The implicit assumption is that a colour distribution arises from a combination of the intrinsic colour spread of a galaxy population, convolved with the measurement error in the contributing filters. A comparison of colour-plots between two surveys, for the same sample, can provide two important statistics: the width of the distribution, and an outlier rate. The 'better' quality data is the data set with the narrowest colour range and the lowest outlier rate (assuming the zero-points are consistent). The colour-plot test is optimal when the intrinsic colour spread is sub-dominant, hence should be made using adjacent filters. In some bands, e.g. (NUV − *u*) the intrinsic colour range is known to be broad (e.g. Robotham & Driver 2011), and hence the test less conclusive. Fig. 21 shows the full set of colour distributions for the GAMA PDR (black histograms), the data have been Galactic extinction corrected but not *k*-corrected, and this is chosen to minimize the modelling dependence, particularly given the wavelength range sampled and uncertainty in *k*-correcting certain regimes (e.g. mid-IR).

Also shown in Fig. 21 is the breadth of the colour distribution derived from the 80 percentile range (horizontal red line and red text) and the median colour value (vertical red line). We derive an outlier rate (indicated by 'Out' as a percentage on the figure), this reports the percentage of galaxies which lie more than 0.5 mag outside the 80 percentile range. The rationale is that the 80 percentile distribution will generally capture the intrinsic+*k*-correction spread, and a catastrophic magnitude measurement would then be one which lies more than 0.5 mag outside of this range. One can see that the colour distributions are particularly broad in the UV bands (as one expects given the range from star-forming systems to inert systems with varying dust attenuation), and in the far-IR bands (as one expects given the range of dust masses and dust temperatures). The red optical and near-IR bands are the narrowest (as expected given the flatness of SEDs at these wavelengths). The outlier rates are generally highest for the poorest resolution and lowest signal-to-noise bands (i.e. NUV, FUV, *u*, and *W*2 onwards) with outlier rates varying from 12.4 to 0.5 per cent. Our ultimate objective within the GAMA survey is to achieve outlier rates below 2 per cent in all bands. With 10 colour distributions at or below this level this implies we have reached this criterion for 11 bands (*g*–*W*1).

The facility cross-over colours, (NUV − *u*), ($z-Z$), ($K-W1$), ($W4-100\,\mu$m), and (160–250 μm), are of particular interest as this is where mis-matches between objects might lead to broader distributions and higher outlier rates, and there is some indication that outlier rates do rise at these boundary points, e.g. the (NUV − *u*) and ($z-Z$) bands and ($K-W1$) bands. In the case of the former, this may simply reflect intrinsic+*k*-correction spread.

No data set sampling a comparable wavelength range currently exists. However, we can compare in the optical and near-IR to the SDSS archive, our previous catalogue (based on SDSS and UKIDSS) and into the UV and mid-IR with the low-*z* templates given in Brown et al. (2014b). These are shown where data exist as blue (GAMA ApMatchedCatv03; SDSS+UKIDSS), green (SDSS DR7 ModelMags), and purple histograms (Brown et al.). Note that as the SDSS and GAMA data are essentially derived from the same base optical data and it is the photometric measurement method which is being tested here. In future, we will be able to compare to KiDS and Subaru Hyper Suprime-Cam (HSC) data sets. In comparison to our previous GAMA catalogue, we can see that PDR represents an improvement (lower breadths and lower outlier rates) in all bands. In particular, the near-IR bands are significantly improved with the colour spread now at least two times narrower. This

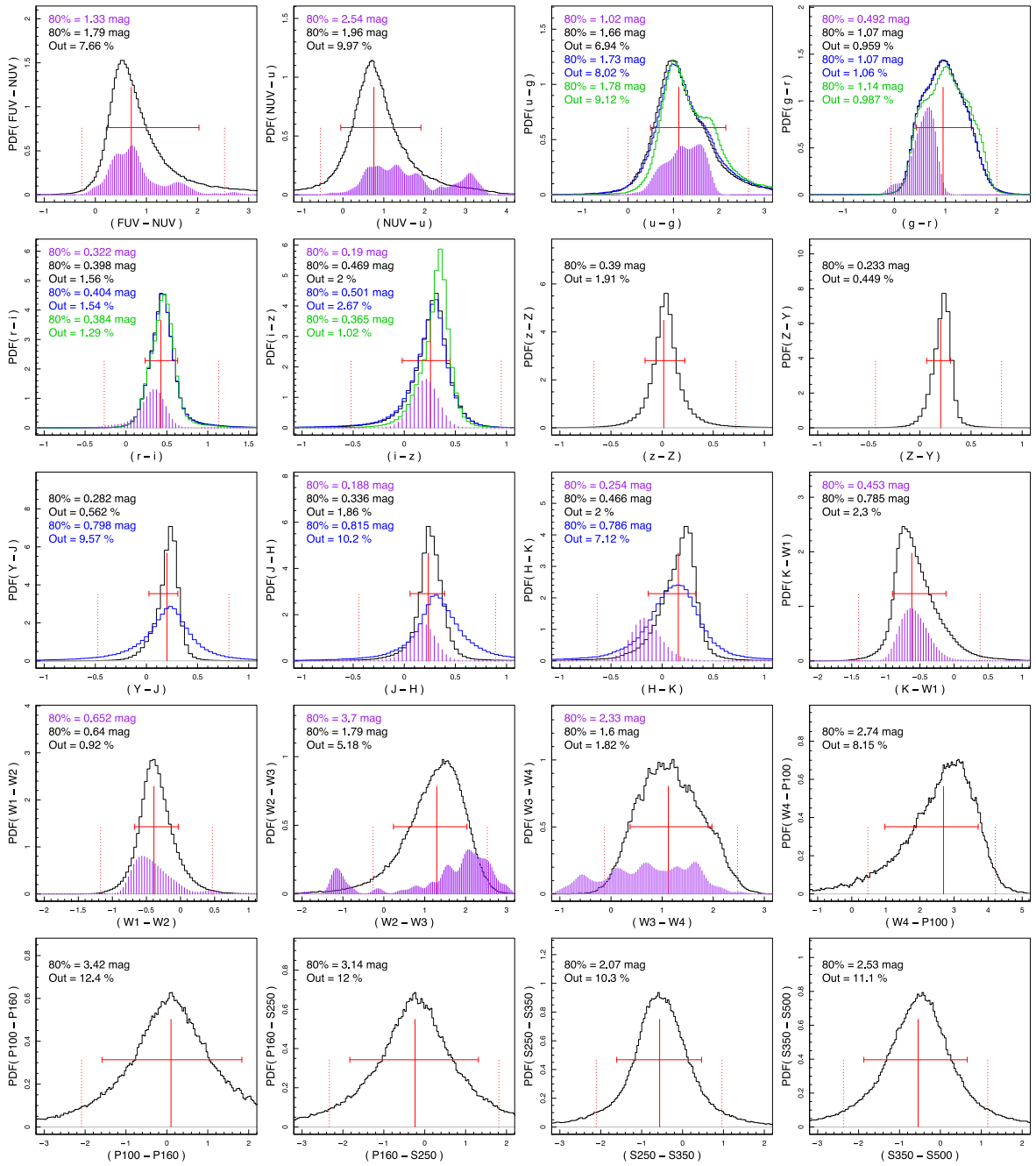

Figure 21. Each panel shows a histogram of a GAMA PDR colour histogram (black distribution) from two adjacent filters (as indicated, y-axis). The horizontal red bar indicates the 80 percentile range of the data with the value for GAMA PDR indicated in black in the top-left corner. The outlier rate (indicated by Out) reports the percentage of the distribution which lies >0.5 mag outside the 80 percentile range (indicated by the vertical dotted lines). Where possible we overlay data from the SDSS DR7 (ModelMag colours, green histograms) and ApMatchedCatv03 (which uses SDSS and UKIDSS data, blue histograms). All distributions are extinction corrected but otherwise as observed. Finally, the shaded histogram (purple) shows data from the $z = 0$ sample of Brown et al. (2014b). However, note that the Brown sample has an ad hoc selection and essentially represent k-band corrected data – hence explaining the apparent discrepancy in (NUV $-$ u), ($u - g$) and ($g - r$), and ($H - K$).

reflects the greater depth of the VIKING data over the UKIDSS LAS data (see Table 3). In comparison to SDSS DR7 ModelMags, we can see that GAMA PDR appears to do marginally better in the ($u - g$) and ($g - r$) colours, but marginally poorer in the ($r - i$) and ($i - z$) bands, in all cases by modest amounts.

Finally, in comparison to the colour distributions derived from the Brown et al. (2014a) templates there are two important caveats. First the Brown data makes no attempt to be *statistically* representative but rather provides an indication of the range of SEDs seen in the nearby population for a relatively ad hoc sample. Secondly the GAMA PDR has a median redshift of $z = 0.24$ and in some bands the k-correction will dominate over the intrinsic distribution. This is apparent in particular in the (NUV $-$ u), ($u - g$), and ($g - r$) bands where the 4000 Å break is redshifted through. This results in significantly broader colours in the observed GAMA PDR colour distributions not seen in the

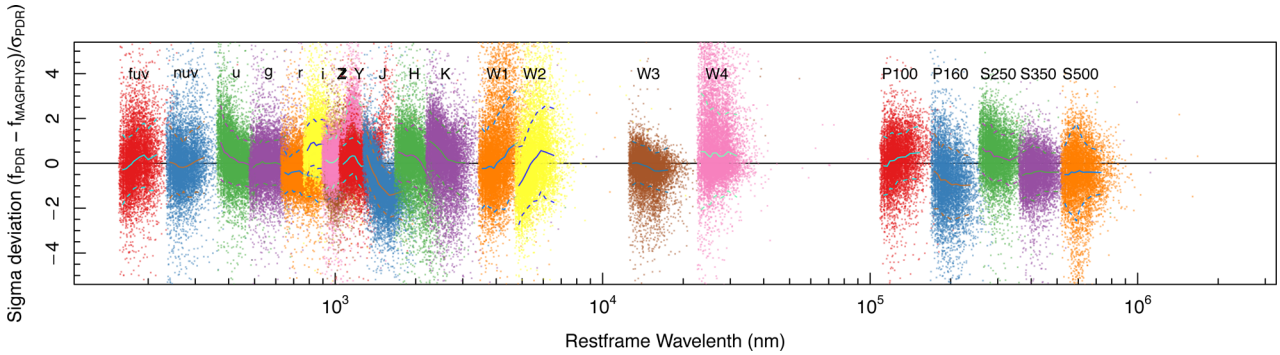

Figure 22. Sigma deviations of the model photometry compared to the input photometry versus rest wavelength for all data points for all galaxies. For each colour, the median and 1σ dispersions is measured and shown (grey solid and dotted lines, respectively). The plot shows that the majority of our data lies within the quoted error of the MAGPHYS fits with some outliers (as also noted in Fig. 21). The offset of *W*4 is of some concern as is the bleeding of the far-IR data towards negative deviation values. Both of these effects are believed to be understood but requires the LAMBDAR software (in development). If these are flat and offset it implies a systematic offset, if they show trends with wavelength it implies a progression of a feature with redshift. Trends are most apparent in the near-IR where the modelling of the TP-AGB population is still uncertain.

rest-frame templates. Again this is understandable. More puzzling is the converse where the $(W2 - W3)$ and $(W3 - W4)$ distributions which are clearly broader in the Brown et al. data. This *may* reflect the incompleteness within the GAMA PDR in these bands, with the bluest objects perhaps being detected in *W*2 but not in *W*3, and hence not represented on these plots (see Cluver et al. 2014 for full discussion on the *WISE* completeness). Similarly for $(W3 - W4)$. For example the Brown et al. sample includes both elliptical systems and very low luminosity blue dwarf systems (e.g. Mrk 331, II Zw 96, Mrk 1490, and UM 461) neither of which would be likely detected by *WISE* at $z \gg 0.01$. The obvious solution is to derive 'forced-photometry' for the full GAMA input catalogue across all bands.

At this point, we believe we have established that GAMA PDR is matching SDSS DR7 ModelMags, a significant improvement over previous GAMA work based on SDSS+UKIDSS LAS, but there remains some concerns regarding higher than desired outlier rates in the lower signal-to-noise and poorer resolution bands, and the need for a measurement at the location of every GAMA galaxy regardless of whether there is obvious flux or not (i.e. forced photometry). Fixing these problems is non-trivial and requires dedicated panchromatic software, which is currently nearing completion and will be presented in Wright et al., (in preparation).

4.1 Composite SEDs

Using a 35 712 core machine available at the Pawsey Supercomputing Centre Facility (MAGNUS), we have now run the MAGPHYS SED fitting code (da Cunha, Charlot & Elbaz 2008), over the full equatorial GAMA sample with redshifts, i.e. 197k galaxies (using the Bruzual & Charlot 2003 spectral synthesis model). MAGPHYS takes as its input, flux measurements in each band, associated errors, and the filter bandpasses, and returns the attenuated and unattenuated SED models from FUV to far-IR, along with a number of physical measurements, e.g. stellar mass, star formation rate, dust mass, dust opacity, dust temperatures (birth-cloud and ISM) etc. (for more details please see da Cunha et al. 2008). Here, we look to use MAGPHYS to provide a simple spectral energy representation for each of our galaxies which also has the effect of filling in the gaps where coverage in a particular band does not exist or no detection is measured. On a single processor MAGPHYS will typically take 10 min to run for a single galaxy (i.e. 4 yr for our full sample), but using MAGNUS the entire sample can be processed in less than 24 h.

Fig. 22 shows each of the $21 \times 197\,491$ data points plotted at the rest wavelength versus the number of σ deviations the GAMA PDR magnitude is away from the derived MAGPHYS magnitude. The figure highlights that generally MAGPHYS appears to be finding consistent fits across all bands with only the *W*4 showing some indication of a fundamental inconsistency between the data and the models. This has now been tracked down to the change in the *W*4 filter transmission curve with our MAGPHYS run still using the old throughput curve while the *WISE* PDR data uses the revised *W*4 transmission curve (see Brown et al. 2014a, for full details). Future runs of MAGPHYS will use the updated curve. The distribution of the data points in σ deviations (abscissa) suggest that the measurement variations are consistent with the errors quoted. The bleed of the far-IR data to the lower part of the figure, is most likely due to contamination by high-z systems (as expected). In the wavelength range, within each filter the near-IR data show the most fluctuations. These are likely to reflect recurrent features in the MAGPHYS models shifting through the various bands and suggests some uncertainty in the precise modelling of the TP-AGB region as noted by numerous groups, e.g. Maraston et al. (2006).

Fig. 23 shows the MAGPHYS SED model fits sampled by our $z < 0.06$ morphologically classified sample, separated into E/S0s (red), Sabcs (green) or Sd/Irrs (blue). See Moffett et al. (2015) for details on the sample and morphological classification process. In order to construct these plots the individual SEDs derived by MAGPHYS have been normalized to the same stellar mass, i.e. their SEDs have been scaled by their fractional stellar mass offset from $10^{10}\,M_*$ (using the stellar masses derived by MAGPHYS). The curves shown are the quantile distributions for 10, 25, 45, 50, 55, 75, and 90 per cent as a function of wavelength. Note that these do not represent individual MAGPHYS SED models, but are quantile ranges in narrow wavelength intervals which are then linked to create the SED quantiles – hence the SEDs show more variations than the models used in MAGPHYS if examined in detail. The reason for this representation is to avoid a specific calibration wavelength and SEDs that, when calibrated into quantiles at one wavelength, cross at others.

Fig. 23 illustrates not only the wealth of data provided by the GAMA PDR but a number of physical phenomena. First, the spread at any wavelength point represents the mass-to-light ratio at that wavelength. This can be seen to be narrowest in the 2–5 μm range

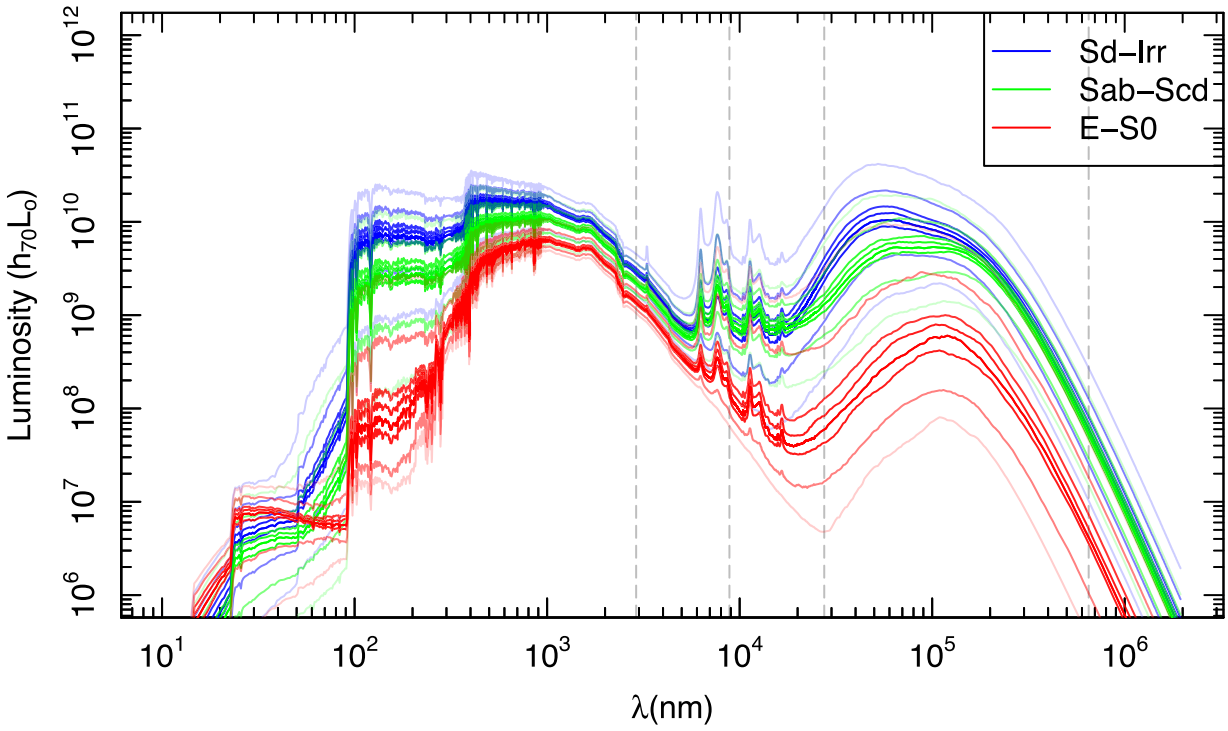

Figure 23. The panel shows the 10, 25,45,50,55,75, and 90 percentiles for the full GAMA PDR SEDs for the $z < 0.06$ morphologically classified sample presented in Moffett et al. (2015). The data are initially scaled to the same mass and then at each wavelength point the quantiles derived which then collectively trace out the quantiles over wavelength. The spread at each wavelength therefore directly reflects the spread in the mass-to-light ratio at that wavelength.

(as expected), indicating that this region is optimal for single band stellar mass estimates. However, the constant gradient in this region implies that near-IR colours provide little further leverage to improve the stellar mass estimation beyond single band measurements. Conversely the smooth variation of SED gradients in the optical from low to high stellar mass ratios, imply that optimal stellar mass estimation may arise from the combination of a single band near-IR measurement combined with an optical colour (see also discussion in Taylor et al. 2011). Fig. 23 highlights the known strong correlations between UV flux, far-IR emission and stellar mass-to-light ratio with all being amplified or suppressed in Sd/Irrs or E/S0s, respectively. However, that all galaxies seem to contain some far-IR emission may be a manifestation of the MAGPHYS code tending to maximize dust content within the bounds as allowed by the far-IR errors. Curiously the Sabc (green) provide a very narrow range of parameters, perhaps indicating a close coupling between star formation, dust production, and the mass-to-light ratio – arguably indicative of well-balanced self-regulated disc formation/evolution. The greater spreads in the early (red) and later (blue) types are perhaps indicative of the progression through various stages of quenching (ramping down) and unstable disc formation (overshoot), respectively. In particular, Agius et al. (2015) found an unexpectedly high levels of dust in a significant (29 per cent) population of the GAMA-E/S0 galaxies consistent with a range of E-So SEDs. Note also the results presented on observed correlations between the star formation rate, specific star formation rate in da Cunha et al. (2010) and Smith et al. (2012), see also interpretation in Hjorth, Gall & Michalowski (2014). A detailed exploration of these phenomena are beyond the scope of this paper but the potential is clear particularly in conjunction with the existing group (Robotham et al. 2011) and large-scale structure (Alpaslan et al. 2014) catalogues.

4.1.1 Inspection of individual objects

We explore individual SEDs for one hundred systems randomly selected (IDs 47500-47609). Approximately 5–10 per cent are found to have one or more significant outlier(s) in the photometry but otherwise good MAGPHYS fits are found for all 100 systems. In approximately 50 per cent of cases the far-IR photometry is essentially missing (due to the shallowness of the far-IR data), hence flux and/or redshift cuts are advisable depending on the science investigation to be conducted. Fig. 24 shows four example galaxies which include a nearby bright system (G47152, $z = 0.082$), a nearby faint system (G47157, $z = 0.074$), a higher redshift crowded system (G47609, $z = 0.282$), and a known far-IR lens system (G622892, $z = 0.300$; Negrello et al. 2010, recently shown to exhibit a spectacular Einstein ring, the very high far-IR flux is evident). The panels on the left show the combined *giH* colour image from a combination of VIKING and SDSS data. Overlaid (green dotted lines) are apertures for the main object and nearby systems in our bright catalogue. The right-hand panels show the 21-band measured photometry (green data and error bars) in units of total energy output (λL_λ in units of h_{70} W) at the filter pivot-wavelength divided by $(1 + z)$ (i.e. rest wavelength). The red and blue lines show the attenuated and unattenuated SEDs from the preliminary MAGPHYS fits. Purple circles show the flux from the attenuated SED curve integrated within the filter bandpasses given in Fig. 1. The lower portion of the panel shows the residuals expressed as the ratio of the observed flux to the measured flux. Included in the error budget is a 10 per cent flux component added in quadrature to mitigate small systematic zero-point offsets at facility boundaries. Comparable plots for all 221k systems with redshifts are provided via the GAMA Ψ online cutout tool (http://gama-psi.icrar.org/).

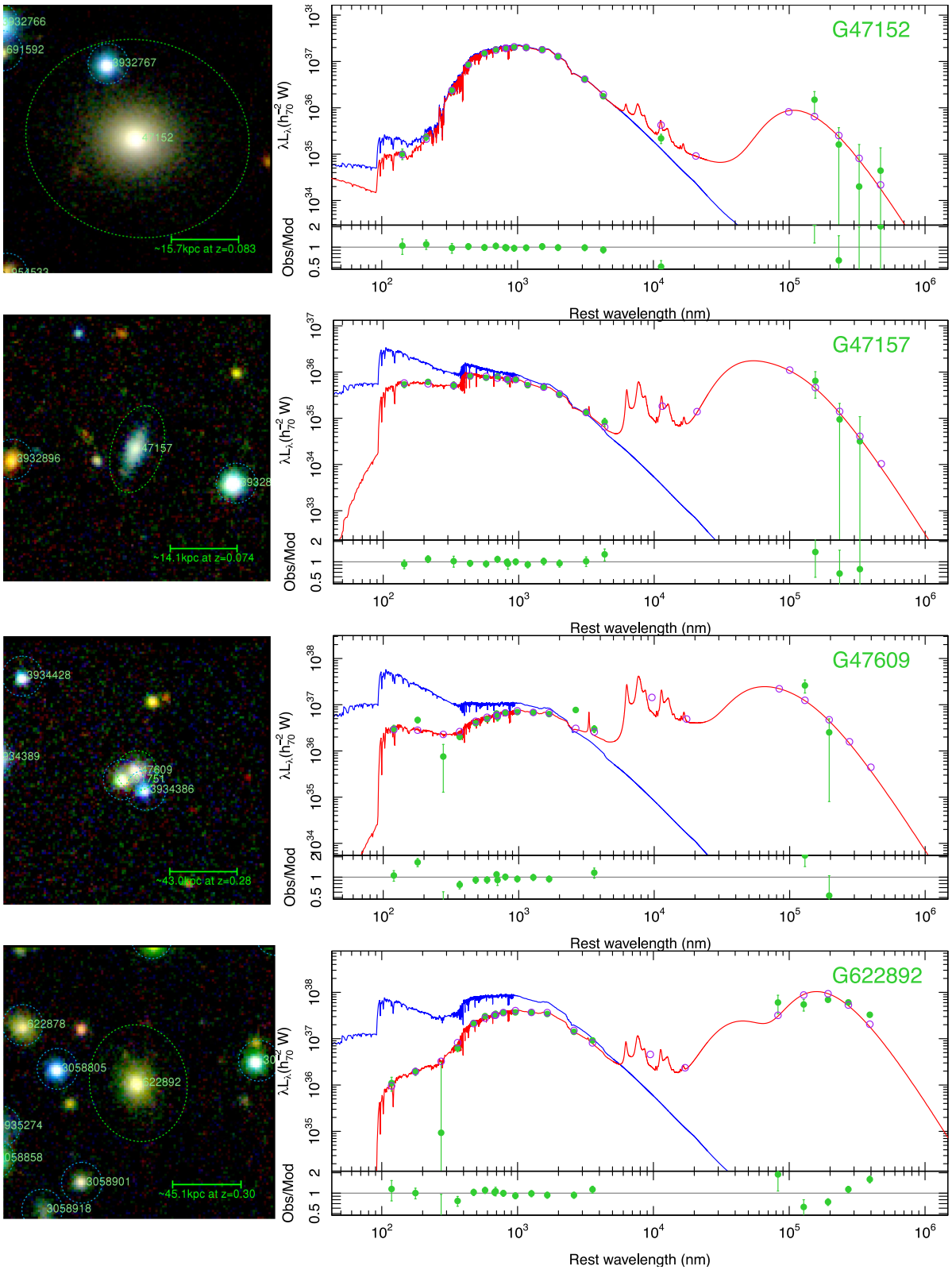

Figure 24. Four example galaxies from the GAMA PDR showing, in each case, the *Hig* image with the apertures overlaid, and the 21-band photometry with the attenuated (red) and unattenuated (blue) MAGPHYS fits to the data. Data shown in green represent the measured photometry plotted at rest wavelength, while the purple circles show the integrated flux measured from the attenuated MAGPHYS fit through the appropriate filter. The lower portion of the main panels shows the residuals, i.e. the ratio of the observed flux to the model flux. Errors include an arbitrary 10 per cent error added in quadrature intended to incorporate some allowance for zero-point offsets between facilities. Note that the lowest image is a well-known lens system reported by Negrello et al. (2010). All images are derived from the GAMA Ψ online cutout tool http://gama-psi.icrar.org/.

The four galaxies are each well sampled by the GAMA PDR data which collectively map out the two key peaks in the energy output due to starlight and dust reprocessing of starlight. The four systems also show varying degrees of dust attenuation with the observed fluxes requiring minimal, significant and extreme corrections to recover the unattenuated fluxes. In all cases, the residuals are well behaved, given the errors. Exploring the GAMA PDR more generally, the SED data appear robust with catastrophic failures in one band typically at the levels indicated in Fig. 21, i.e. 10 per cent in poorly resolved bands to 1 per cent in well-resolved bands. Obvious issues which arise following inspection of several hundred SEDs are: incorrect apertures, data artefacts (i.e. poor-quality regions), nearby bright stars (diffraction spikes and blocking), crowding, and confusion.

5 THE ENERGY OUTPUT OF THE UNIVERSE AT $z < 0.2$ FROM FUV TO FAR-IR

We conclude this paper with a brief look at the integrated energy output of the low-redshift galaxy population, i.e. the cosmic spectral energy distribution (CSED), its recent evolution, and the implied integrated photon escape fraction (IPEF). The CSED represents the energy output of a cosmologically representative volume, in essence an inventory of the photons recently generated, as opposed to those passing through but formed earlier. It can be reported both pre- and post-attenuation by the dust content of the galaxy population, both are interesting. The pre-attenuated CSED informs us of the photons being created from (primarily) nucleosynthesis processes (in the current epoch), while the post-attenuated CSED informs us of the photons entering into the IGM. The sum of the two must equal (energy conservation), but the wavelength distribution will differ as dust re-processes the emergent photons from short (UV and optical) to long (mainly far-IR) wavelengths. The combination of the two can be used to determine the IPEF. By integrated we imply over a representative galaxy population, and averaged over representative viewing angles. Both of these factors are important and make the IPEF useful for converting observed FUV and NUV fluxes to robust star formation rates. The work follows earlier measurements of the CSED reported in Driver et al. (2008) and Driver et al. (2012). However, the methodology here is very different and for the first time includes mid- and far-IR data in a fully consistent analysis. In our earlier studies, we determined luminosity distributions in each band independently and then fitted across these values to determine the CSED. Here we stack the individual MAGPHYS SEDs fits derived earlier, as representative fitting functions (see Fig. 24).

Potentially, as we have a MAGPHYS fit for every galaxy we could use them to derive fluxes in data gaps and use the full sample. However, given the critical importance of the far-IR dust constraint we elect to use just the common region with full 21-band coverage (see Figs A1–A4). This combined region constitutes an area of 63 per cent of the full area or 113 deg^2 and contains 138k objects with secure redshifts in the range $0.02 < z < 0.5$ (trimmed to exclude stars and high-z AGN). To explore any evolution of the CSED, we divide our sample into three redshift intervals: $0.02 < z < 0.08$, $0.08 < z < 0.14$, and $0.14 < z < 0.2$ which correspond roughly to lookback times of 0.8, 1.5, and 2.25 Gyr, respectively. The volumes sampled are: 4.9×10^5, 2.1×10^6, and $4.6 \times 10^6\, h_{70}^{-3}$ Mpc^3, respectively (factoring in our reduced coverage). Within each redshift range we use the $z_{\rm max}$ values reported in Taylor et al. (2011) to derive a weight as not all galaxies would be visible across the selected redshift range. Galaxies with $z_{\rm max}$ values above the redshift range have weights set to unity, and values with $z_{\rm max}$ below this range have weights set to zero. Otherwise weights are set to the inverse of the fraction of the volume sampled. A cap is placed ensuring no weight exceeds a value of 10, this ensures a single lone system just fortuitously within the redshift range cannot dominate the final outcome by being massively amplified. Within each redshift range, we now simply sum the energy $\times$ weight (i.e. $\sum W_i \lambda L_\lambda^i$) for the galaxies within our selection to arrive out the CSED for that volume.

These raw derived CSEDs require one final correction to accommodate for the loss of lower luminosity systems in the higher redshift bins. To determine the correction factor we repeat the summation but with a stellar mass cut imposed on all three samples (10^{10} M$_\odot$), this is sufficiently low to be sampling the dominant contribution to the CSED but not so low as to suffer total incompleteness (i.e. that which is not corrected for by our weights). For each volume interval we obtain unrestricted to mass-restricted CSED ratios of: 1.68, 1.48, and 1.29 for the low-, mid-, and high-redshift samples, respectively. If all three samples were complete this ratio would be constant, hence this changing ratio encodes the loss of the lower luminosity systems in the higher redshift bins, and can therefore be used to provide an appropriate correction. This is achieved by scaling the final CSED curves by factors of 1.00, 1.14 (i.e. 1.68/1.48), and 1.30 (i.e. 1.68/1.29), respectively. In effect we are using the CSED shape from the unrestricted samples but normalizing using the restricted samples and this is analogous to the normalizations typically used in estimating luminosity and mass functions. This implicitly assumes the following: that the low-redshift sample is itself complete (hence requiring no scaling), and that the ratio of energy emerging from systems above and below 10^{10} M$_\odot$ is approximately constant. The first of these is relatively secure: GAMA is a deep survey and at $z \sim 0.08$ is mass complete to 10^9 M$_\odot$ (see Lange et al. 2015), below which there is very little contribution to the luminosity density (see Driver 1999), or stellar mass density (see Moffett et al. 2015). In the second case, we understand low-mass systems are preferentially star forming and may have evolved more rapidly over recent times compared to the more massive systems. However, as the correction factors are relatively modest (14 and 30 per cent) the shape and renormalization is unlikely to be dramatically changed, but we acknowledge may be biased low. This can only be quantified through deeper studies (see for example the planned WAVES survey; Driver et al. 2015).

Fig. 25 shows the resulting energy outputs for the renormalized unattenuated CSED (upper) and the renormalized attenuated CSED (lower) with the redshift ranges represented by colour as indicated. Also shown is our earlier estimate derived from GAMA via luminosity function fitting (orange line). It is worth re-iterating that the Driver et al. (2012) CSED measurement is based on luminosity density measurements from FUV to K_s combined with an adopted IPEF (Driver et al. 2008) to infer the mid and far-IR portion, i.e. the mid- and far-IR from Driver et al. (2012) is a prediction, and hence shown as a dotted line beyond 2.1 μm. Also shown is the prediction from semi-analytic modelling by Somerville et al. (2012). Both curves, corrected to $H_o = 70$ km s^{-1} Mpc^{-1}, follow the new low-z CSED very well in the optical and start to diverge in the mid- and far-IR bands where previous empirical data have been lacking. The Somerville curve, in particular traces the low-redshift bin extremely well with the previous Driver data significantly underpredicting the far-IR emission. The CSEDs presented here represent a major advance constituting the first consistent measurement of the post-attenuated CSED from a single sample spanning from the FUV to far-IR. Hence, while cosmic (sample) variance (CV) may scale the respective CSEDs in overall density, it will not modify the shape of the distribution (unless there are extreme hidden clustering

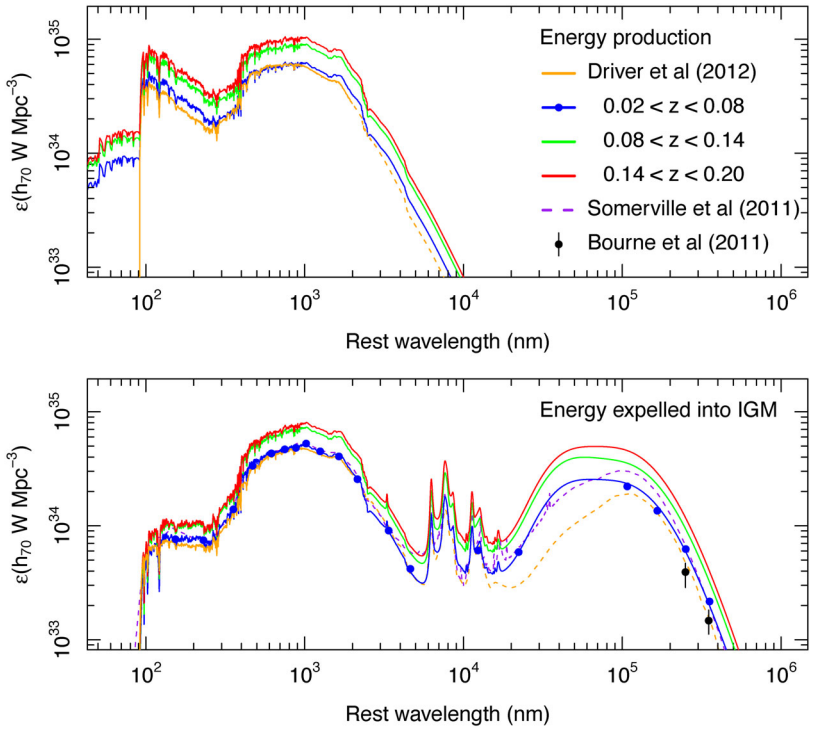

Figure 25. The energy originating (i.e. unattenuated, top), and emanating (i.e. attenuated following dust reprocessing, lower) at intervals equivalent to 0.75, 1.5, and 2.25 Gyr lookback time. The data are normalized to the energy output per Mpc^3 for $H_o = 70$ km s^{-1} Mpc^{-1}. The data show clear trends in the evolution of the total energy output over this timeline.

factors). Using the formula in Driver & Robotham (2010, see also the online calculator http://cosmocalc.icrar.org/), we derive the CV, for our three redshift ranges to be: 18, 12, and 10 per cent, respectively, with increasing redshift and note that despite the extent of the GAMA PDR the dominant error remains the CV.

To first order the CSEDs are therefore all consistent with each other and the previous values. The CSEDs follow the expected progression towards higher energy output towards higher redshifts, despite the potential uncertainty in overall normalization from CV. In particular the far-IR increases noticeably faster than the optical. This result is independent of CV and noted previously within the far-IR community, see for example Dunne et al. (2011) who infer a significant increase in dust mass (towards high redshift) over the past 5 Gyr. In detail we can report that the Universe is in energy decline, having dropped from a total energy production of $(2.5 \pm 0.2) \times 10^{35}\, h_{70}$ W Mpc^{-3} at 2.25 Gyr ago, to $(2.2 \pm 0.2) \times 10^{35}\, h_{70}$ W Mpc^{-3} at 1.5 Gyr ago and $(1.5 \pm 0.3) \times 10^{35}\, h_{70}$ W Mpc^{-3} at 0.75 Gyr ago. This decline is significant despite the CV uncertainty, and in line with our understanding of the evolution in the cosmic star formation history (e.g. Hopkins & Beacom 2006), which shows a decline of a factor of approximately $\times$ 1.5 over this time frame. The lowest redshift bin value is also consistent with the $(1.26 \pm 0.09) \times 10^{35}\, h_{70}$ W Mpc^{-3} for $z < 0.1$ as reported in Driver et al. (2012) and the orange and blue curves on Fig. 25 do show consistency over the optical regime. The majority of the energy difference is derived from the far-IR where previous data were lacking and the CSED in this region estimated. As an aside it is also worth noting that the near-IR data show some slight disagreement, and this is consistent with our finding that VIKING fluxes are typically brighter than UKIDSS LAS fluxes (see Section 3.4). Finally, shown in Fig. 25 are the SPIRE data points derived by the *Herschel*-ATLAS team from the initial data release which sampled all of G09, G15, and half of G12 (Bourne et al. 2012). These data are low compared to our new estimate, however the SPIRE calibration and data reduction have evolved quite substantially since these data points were derived.

Integrating these distributions reveals some interesting numbers. From the unattenuated CSED, we find that 50 per cent of the energy production in the nearby Universe is at wavelengths in the range 0.01–0.64 μm (i.e. UV/optical). In the post-attenuated 'observed' CSED, 50 per cent of the energy emerges at wavelengths shorter than 1.7 μm. Splitting at 10 μm we find that 65 per cent of the energy produced (via stellar emission) is released into the IGM at shorter wavelengths and 35 per cent at longer wavelengths. Despite dust contributing a very small proportion of a galaxy's mass (typically $<$1 per cent; Driver et al. 2008), its impact on the energy output is dramatic with significant potential consequences for optically based flux and size measurements (see for example Pastrav et al. 2013).

Dividing the pre- and post-attenuated CSEDs yields the IPEF. This is a particularly interesting distribution as it encapsulates the impact of dust in a simple and general way. Fig. 26 shows the IPEF in the three redshift bins. Also shown (purple diamonds) is the IPEF derived in Driver et al. (2008) for the Millennium Galaxy Catalogue (Liske et al. 2003). Clearly apparent is a trend towards lower photon escape fractions towards modestly higher redshift, demonstrating the impact of dust evolution in our perception of even low-redshift systems ($z < 0.2$). It is important to note that this result is resilient to CV as we are comparing the ratio of the pre- and post-attenuated CSEDs and hence the normalization cancels out. The variation appears smooth with redshift and significant, with the escape fraction in the FUV changing from 18 per cent in the higher redshift bin to 23 per cent in the lower z bin. The corresponding change in the NUV is 27–34 per cent, respectively. If this trend continues the implication is that at even intermediate redshifts the UV photon escape fraction may be significantly lower

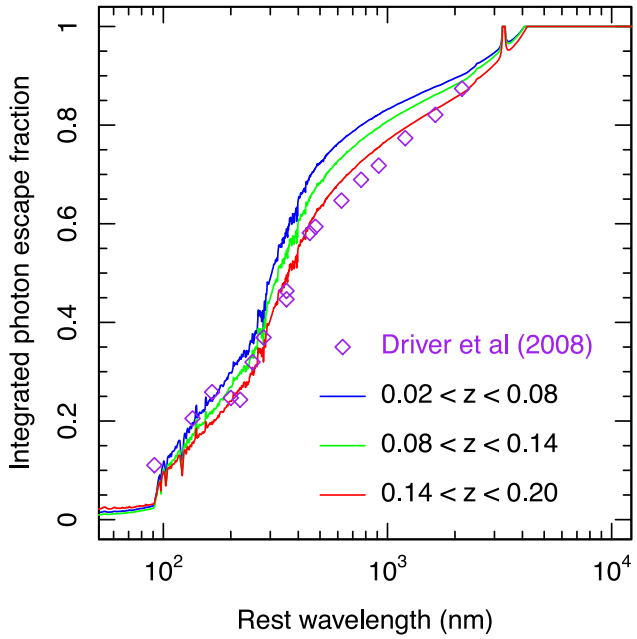

Figure 26. The photon escape fraction integrated over all viewing angles and derived from Fig. 25. Also shown is the escape fraction reported by Driver et al. (2008) from the Millennium Galaxy Catalogue within the redshift range $0.0 < z < 0.18$. The data show a clear progression towards lower escape fractions as redshift increases.

than the values typically adopted when deriving star formation rates from UV fluxes.

The above work should be considered as preliminary, but indicative of the potential of the GAMA PDR to explore the energy outputs of galaxies and galaxy population at low redshift. The analysis at present also includes a number of important caveats which we are looking to address in the near future. The first is outstanding issues related to the GAMA photometry: aperture robustness, the need for a uniform forced photometry across all bands, and improved management of the variable spatial resolutions and signal-to-noise limits. The second is whether MAGPHYS provides truly unbiased fits, particularly in the far-IR where our data quality is lowest and where, as the errors grow, overfitting of the far-IR fluxes cannot be ruled out. Verifying that MAGPHYS is unbiased will be important as our data quality undoubtedly declines with redshift. One should also bear in mind that the interpretations above are very much based on the assumptions embedded in the MAGPHYS code, in due course it will be important to explore a range of assumptions and to undertake critical comparisons against fully radiative transfer codes for well-resolved systems. The third and arguably most fundamental issue relates back to the integrity of the GAMA input catalogue and in particular its reliance on the fairly shallow SDSS imaging and the potential for missing extended low surface brightness systems. The GAMA regions are currently being surveyed by the VST KiDS team and will also be surveyed as part of the HSC Wide survey, both data sets can be used to improve our input catalogue particularly for extended low surface brightness systems.

6 SUMMARY

We have brought together a number of diverse data sets from three space missions (*GALEX*, *WISE,* and *Herschel*), and two ground-based facilities (SDSS and VISTA) to produce the GAMA PDR. The individual data frames have been astrometrically and photometrically matched, and then SWarped into single images for each of the three equatorial GAMA regions covering 80 deg^2 each (i.e. slightly larger than the nominal 60 deg^2 region covered by the spectroscopy). Weight maps are provided indicating the number of frames contributing to each region and files containing the names of the individual frames used. In the $u - K_s$ bands, we provide both native resolution data and data degraded to a common 2 arcsec FWHM. The SWarped images along with a cutout tool (GAMA Ψ) for extracting subregions are available at: http://gama-psi.icrar.org/. Note that the *Herschel* data are currently proprietary but will be made available following the *Herschel*-ATLAS final data release.

GAMA Ψ also provides additional functionality to create colour images on the fly from the combination of any of the 21-bands, individual fits downloads, object and aperture overlays and is maintained by the International Centre for Radio Astronomy Research (ICRAR) Data Intensive Astronomy unit. Queries and comments on GAMA Ψ should be sent to simon.driver@uwa.edu.au.

We describe the construction of the $u - K_s$ aperture-matched photometry following the method described in Hill et al. (2011) and compare to our previous measurements. In addition, we compare our near-IR photometry for 400k stars extracted from 2MASS and confirm that our zero-points are robust to within a tenth of a magnitude.

The VIKING-2MASS and UKIDSS-2MASS zero-points are shown to be robust, however VIKING-UKIDSS photometry do not agree. This apparent tautological inconsistency is most likely explained by a linearity issue as the VIKING and UKIDSS data are compared at a significantly fainter magnitude range. Some evidence is seen for a linearity issue in the UKIDSS-2MASS comparison, which when extrapolated to fainter magnitudes does appear to explain the offsets seen between VIKING and UKIDSS.

We also describe our method for deriving far-IR measurements using optical priors where we use our *r*-band apertures convolved with the appropriate instrument/filter PSF to measure the far-IR flux at the location of every object.

We then combine our $u - K_s$ and 100-500 μm fluxes with *GALEX* and *WISE* data derived by the MPIK and UCT/UWC groups led by RJT and MC using exact name ID matching. This results in a final catalogue of over 221k objects from the G09, G12, G15, and G23 regions, 63 per cent of which have complete coverage in all 21 bands.

Finally, as a demonstration of this data set we derive the total flux originating and emanating from various volumes from FUV to far-IR at redshifts indicative of 0.8, 1.5, and 2.25 Gyr lookback time. We see evidence for evolution over this period consistent with the decline of star formation traced by the cosmic star formation history and consistent with the reported evolution of the far-IR Luminosity Functions (LFs).

In future papers, we will further improve our flux extraction method using optically motivated priors in all bands, leading to more consistent errors, and explore the physical properties derived from SED fitting codes for various populations and sub-populations.

ACKNOWLEDGEMENTS

LD and SJM acknowledge support from the European Advanced Investigator grant cosmicism. SB acknowledges support from an ARC Future Fellowship (FT140101166). NB acknowledges support from EC FP7 SPACE project ASTRODEEP (Ref. No: 312725). EI acknowledges funding from CONICYT/FONDECYT post-doctoral project no: 3130504. MALL acknowledges support from UNAM through PAPIIT project IA101315. PN acknowledges the support

of the Royal Society through the award of a University Research Fellowship, the European Research Council, through receipt of a Starting Grant (DEGAS-259586) and support of the Science and Technology Facilities Council (ST/L00075X/1).

We acknowledge the use of data products from the NASA operated *GALEX* space mission. We also acknowledge the following institutions and agencies for their financial contributions towards the reactivation and operations of the *GALEX* satellite. This has allowed us to complete NUV observations of the G23 and *Herschel* ATLAS SGP regions: the Australian-Astronomical Observatory (AAO), the Australian Research Council (ARC), the International Centre for Radio Astronomy Research (ICRAR), the University of Western Australia, the University of Sydney, the University of Canterbury, Max-Plank Institute für KernPhysik (MPIK), the University of Queensland, the University of Edinburgh, Durham University, the European Southern Observatory (ESO), the University of Central Lancashire, Liverpool John Moore University, National Aeronautics and Space Administration (NASA), Université Paris Sud, University of California Irvine, Instituto Nazionale Di Astrofisica (INAF), and the University of Hertfordshire.

Funding for the SDSS and SDSS-II has been provided by the Alfred P. Sloan Foundation, the Participating Institutions, the National Science Foundation, the US Department of Energy, the National Aeronautics and Space Administration, the Japanese Monbukagakusho, the Max Planck Society, and the Higher Education Funding Council for England. The SDSS website is http://www.sdss.org/.

The SDSS is managed by the Astrophysical Research Consortium for the Participating Institutions. The Participating Institutions are the American Museum of Natural History, Astrophysical Institute Potsdam, University of Basel, University of Cambridge, Case Western Reserve University, University of Chicago, Drexel University, Fermilab, the Institute for Advanced Study, the Japan Participation Group, Johns Hopkins University, the Joint Institute for Nuclear Astrophysics, the Kavli Institute for Particle Astrophysics and Cosmology, the Korean Scientist Group, the Chinese Academy of Sciences (LAMOST), Los Alamos National Laboratory, the Max-Planck-Institute for Astronomy (MPIA), the Max-Planck-Institute for Astrophysics (MPA), New Mexico State University, Ohio State University, University of Pittsburgh, University of Portsmouth, Princeton University, the United States Naval Observatory, and the University of Washington.

The VIKING survey is based on observations with ESO Telescopes at the La Silla Paranal Observatory under the programme ID 179.A-2004.

This publication makes use of data products from the *WISE*, which is a joint project of the University of California, Los Angeles, and the Jet Propulsion Laboratory/California Institute of Technology, funded by the National Aeronautics and Space Administration.

The *Herschel*-ATLAS is a project with *Herschel*, which is an ESA space observatory with science instruments provided by European-led Principal Investigator consortia and with important participation from NASA. The H-ATLAS website is http://www.h-atlas.org/.

GAMA is a joint European–Australasian project based around a spectroscopic campaign using the Anglo-Australian Telescope. The GAMA input catalogue is based on data taken from the SDSS and the UKIRT Infrared Deep Sky Survey. Complementary imaging of the GAMA regions is being obtained by a number of independent survey programmes including *GALEX* MIS, VST KiDS, VISTA VIKING, *WISE*, *Herschel*-ATLAS, GMRT and ASKAP providing UV to radio coverage. GAMA is funded by the STFC (UK), the ARC (Australia), the AAO, and the participating institutions. The GAMA website is http://www.gama-survey.org/.

This work is supported by resources provided by the Pawsey Supercomputing Centre with funding from the Australian Government and the Government of Western Australia.

REFERENCES

Abazajian K. N. et al., 2009, ApJS, 182, 543
Agius N. et al., 2015, MNRAS, 451, 3815
Alpaslan M. et al., 2014, MNRAS, 438, 177
Andrae E., 2014, PhD thesis, MPIfK
Arnaboldi M. et al., 2007, Messenger, 127, 28
Baldry I. K. et al., 2010, MNRAS, 404, 86
Barnes D. G. et al., 2001, MNRAS, 322, 486
Bate M., Bonnell I. A., Bromm V., 2003, MNRAS, 339, 577
Bertin E., 2010, Astrophysics Source Code Library, record ascl.1010.068
Bertin E., 2011, in Evans I. N., Accomazzi A., Mink D. J., Rots A. H., eds, Proc. ASP Conf. Ser. Vol. 442, Astronomical Data Analysis Software and Systems XX. Astron. Soc. Pac., San Francisco, p. 435
Bourne N. et al., 2012, MNRAS, 421, 3027
Brown M. J. I., Jarrett T. H., Cluver M. E., 2014a, PASA, 31, 49
Brown M. J. I. et al., 2014b, ApJS, 212, 18
Bruzual G., Charlot S., 2003, MNRAS, 344, 1000
Calzetti D., Armus L., Bohlin R. C., Kinney A. L., Koornneef J., Storichi-Bergmann T., 2000, ApJ, 533, 682
Cluver M. et al., 2014, ApJ, 782, 90
da Cunha E., Charlot S., Elbaz D., 2008, MNRAS, 388, 1595
da Cunha E., Eminian C., Charlot S., Blaizot J., 2010, MNRAS, 403, 1894
Dalton G. et al., 2006, in McLean I. S., Iye M., eds, Proc. SPIE Conf. Ser. Vol. 6269, Ground-based and Airborne Instrumentation for Astronomy, SPIE, Bellingham, p. 62690X
de Jong J. T. A., Verdoes Kleijn G. A., Konrad K. H., Valentijn E. A., 2013 Exp. Astron., 35, 25
Domínguez A. et al., 2011, MNRAS, 410, 2556
Drinkwater M. J. et al., 2010, MNRAS, 401, 1429
Driver S. P., 1999, ApJ, 526, 69
Driver S. P., Popescu C. C., Tuffs R. J., Liske J., Graham A. W., Allen P. D., de Propris R., 2007, MNRAS, 379, 1022
Driver S. P., Popescu C. C., Tuffs R. J., Graham A. W., Liske J., Baldry I., 2008, ApJ, 678, 101
Driver S. P. et al., 2009, Astron. Geophys., 50, 12
Driver S. P. et al., 2011, MNRAS, 413, 971
Driver S. P. et al., 2012, MNRAS, 427, 3244
Driver S. P., Davies L. J., Meyer M., Power C., Robotham A. S. G., Baldry I. K., Liske J., Norberg P., 2015, ASSP, in press (arXiv: 1507.00676)
Dunne L. et al., 2011, MNRAS, 417, 1510
Eales S. et al., 2010, PASP, 122, 499
Edge A., Sutherland W., Kuijken K., Driver S. P., McMahon R., Eales S., Emerson J. P., 2013, The Messenger, 154, 32
Fontanot F., Monaco P., Cristiano S., Tozzi P., 2006, MNRAS, 373, 1173
Giavalisco M. et al., 2004, ApJ, 600, 93
Griffin M. J. et al., 2010, A&A, 518, 232
Grogin N. A. et al., 2011, ApJS, 197, 35
Hambly N. C. et al., 2001, MNRAS, 326, 1279
Hill D., Driver S. P., Cameron E., Cross N., Liske J., Robotham A., 2010, MNRAS, 404, 1215
Hill D. et al., 2011, MNRAS, 412, 765
Hjorth J., Gall C., Michalowski M. J., 2014, MNRAS, 782, 23
Hopkins A. M., Beacom J. F., 2006, ApJ, 651, 142
Hopkins P. F., Hernquist L., Cos T. J., Di Matteo T., Robertson B., Springel V., 2006, ApJS, 163, 1
Hopkins A. M. et al., 2013, MNRAS, 430, 2047
Ibar E. et al., 2010, MNRAS, 409, 38
Jarrett T. H. et al., 2012, AJ, 144, 68
Jarrett T. H. et al., 2013, AJ, 145, 6
Kelvin L. et al., 2012, MNRAS, 421, 1007
Kelvin L. et al., 2014, MNRAS, 444, 1647

Kennicutt R. C. et al., 2003, PASP. 115, 928
Keres D., Katz N., Weinberg D, Davé R., 2005, MNRAS, 363, 2
Koekemoer A. M. et al., 2011, ApJS, 197, 36
Komatsu E. et al., 2011, ApJS, 192, 18
Lacey C., Cole S., 1993, MNRAS, 262, 627
Lange R. et al., 2015, MNRAS, 447, 2603
Lewis J. R., Irwin M., Bunclark P., 2010, in Mizumoto Y., Morita K.-I., Ohishi M., eds, Proc. ASP Conf. Ser. Vol. 434, Astronomical Data Analysis Software and Systems XIX. Astron. Soc. Pac., San Francisco, p. 91
Liske J., Lemon D. J., Driver S. P., Cross N. J. G., Couch W. J., 2003, MNRAS, 344, 307
Liske J. et al., 2015, MNRAS, 452, 2087
McKee C. F., Ostriker E. C., 2007, ARA&A, 45, 565
Maraston C., Daddi E., Renzini A., Cimatti A., Dickinson M., Papovich C., Pasquali A., Pirzkal N., 2006, ApJ, 652, 82
Martin C. et al., 2005, ApJ, 619, 1
Masci F. J., 2013, Astrophysics Source Code Library, record ascl:1302.010, preprint (arXiv:1301.2718)
Masci F. J., Fowler J. W., 2009, in Bohlender D. A., Durand D., Dowler P., eds, Proc. ASP Conf. Ser. Vol. 411, Astronomical Data Analysis Software and Systems XVIII. Astron. Soc. Pac., San Francisco, p. 67
Moffett A. et al., 2015, MNRAS, submitted
Morrissey P. et al., 2007, ApJS, 173, 682
Munoz-Mateos J. C. et al., 2015, ApJS, 219, 3
Negrello et al., 2010, Science, 330, 800
Pascale E. et al., 2011, MNRAS, 415, 911
Pastrav B., Popescu C. C., Tuffs R. J., Sansom A. E., 2013, A&A, 557, 137
Pilbratt G. L. et al., 2010, A&A, 518, 1
Poglitsch A. et al., 2010, A&A, 518, 2
Popescu C. C., Tuffs R. J., 2002, MNRAS, 335, 41
Rigby E. E. et al., 2011, MNRAS, 415, 2336
Robotham A. S. G., Driver S. P., 2011, MNRAS, 413, 2570
Robotham A. S. G. et al., 2010, PASA, 27, 76
Robotham A. S. G. et al., 2011, MNRAS, 416, 2640
Rowlands K. et al., 2012, MNRAS, 419, 2545
Schlegel D. J., Finkbeiner D. P., Davis M., 1998, ApJ, 500, 525
Schoenberner D., 1983, ApJ, 272, 708
Scoville N. et al., 2007, ApJS, 172, 1
Sheth K. et al., 2010, PASP, 122, 1397
Shu F., Adams F. C., Lizano S., 1987, ARA&A, 25, 23
Skrutskie M. F. et al., 2006, AJ, 131, 1163
Smith D. et al., 2011, MNRAS, 416, 857
Smith D. et al., 2012, MNRAS, 427, 703
Soifer B. T., Neugenbauer G., Hoick J. R., 1987, ARA&A, 25, 187
Somerville R. S., Gilmore R. C., Primack J. R., Domínguez A., 2012, MNRAS, 423, 1992
Soto M. et al., 2013, A&A, 552, 101
Sutherland R. et al., 2015, A&A, 575, 25
Taylor N. et al., 2011, MNRAS, 418, 1587
Tinsley B., 1980, Fundam. Cosm. Phys., 5, 287
Toomre A., Toomre J., 1972, ApJ, 178, 623
Tuffs R. J., Popescu C. C., Völk H. J., Kylafis N. D., Dopita M. A., 2004, A&A, 419, 821
Veilleux S., Cecil G., Bland-Hawthorn J., 2005, ARA&A, 43, 769
White S. D. M., Rees M. J., 1978, MNRAS, 183, 341
White R. L., Becker R. H., Helfand D. J., Gregg M. D., 1997, ApJ, 475, 479
Wright E. L. et al., 2010, AJ, 140, 1868
York D. et al., 2000, AJ, 120, 1579

APPENDIX A: GAMA PDR COVERAGE

Figs A1–A4 shows the GAMA PDR coverage in each of the 21 bands, all data are available for download via: http://gama-psi.icrar.org/.

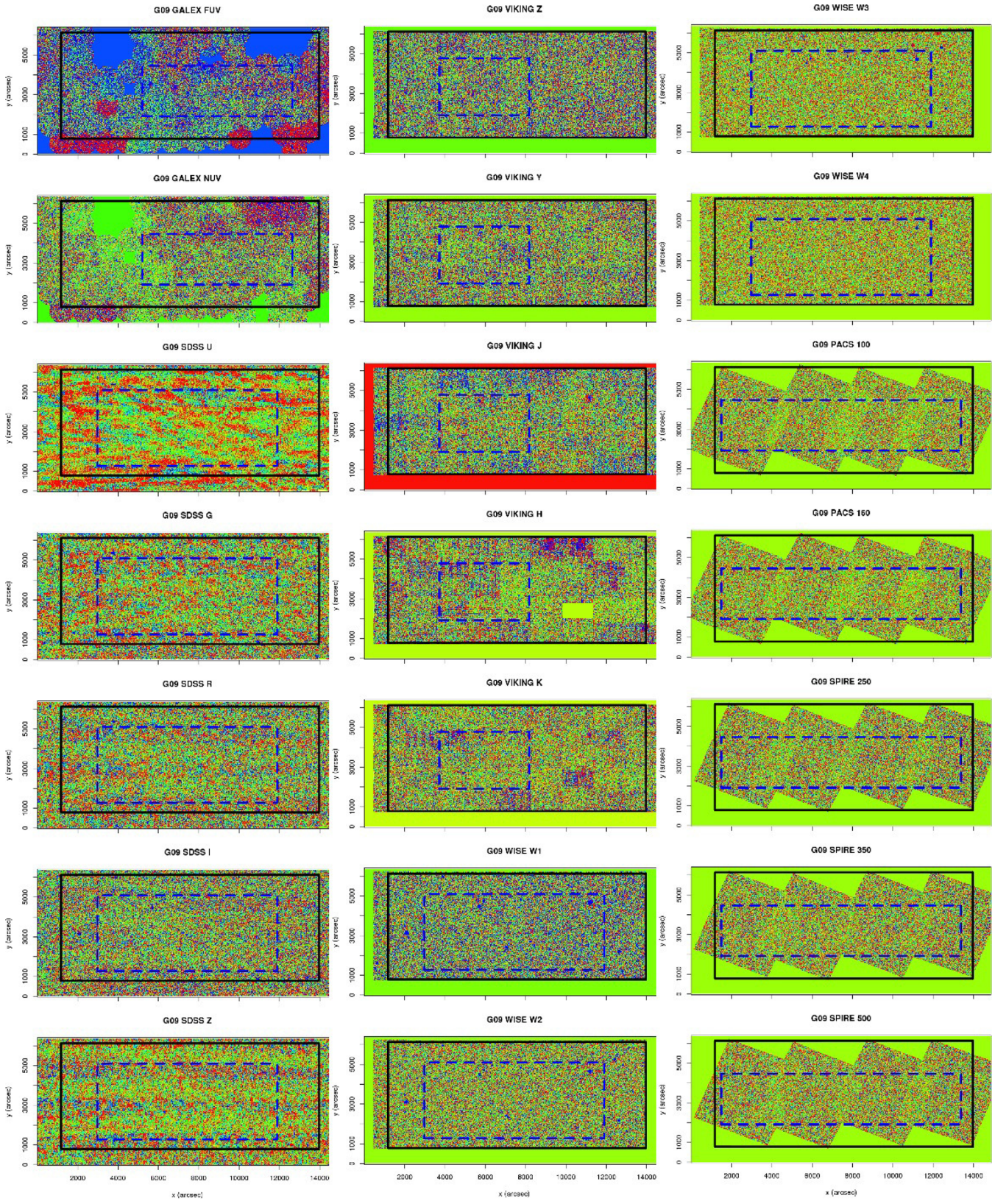

Figure A1. Background uniformity and coverage in the G09 region for *GALEX*, SDSS, VIKING, *WISE,* and *Herschel* data. The black box denotes the GAMA spectroscopic survey region and the blue box the region from which the background statistics were derived. We use the MOGRIFY package to display the low-res data frames very close to the sky level. Astronomical objects will not be visible, however the frames highlight the coverage, missing regions, and the integrity of the large-scale sky structure.

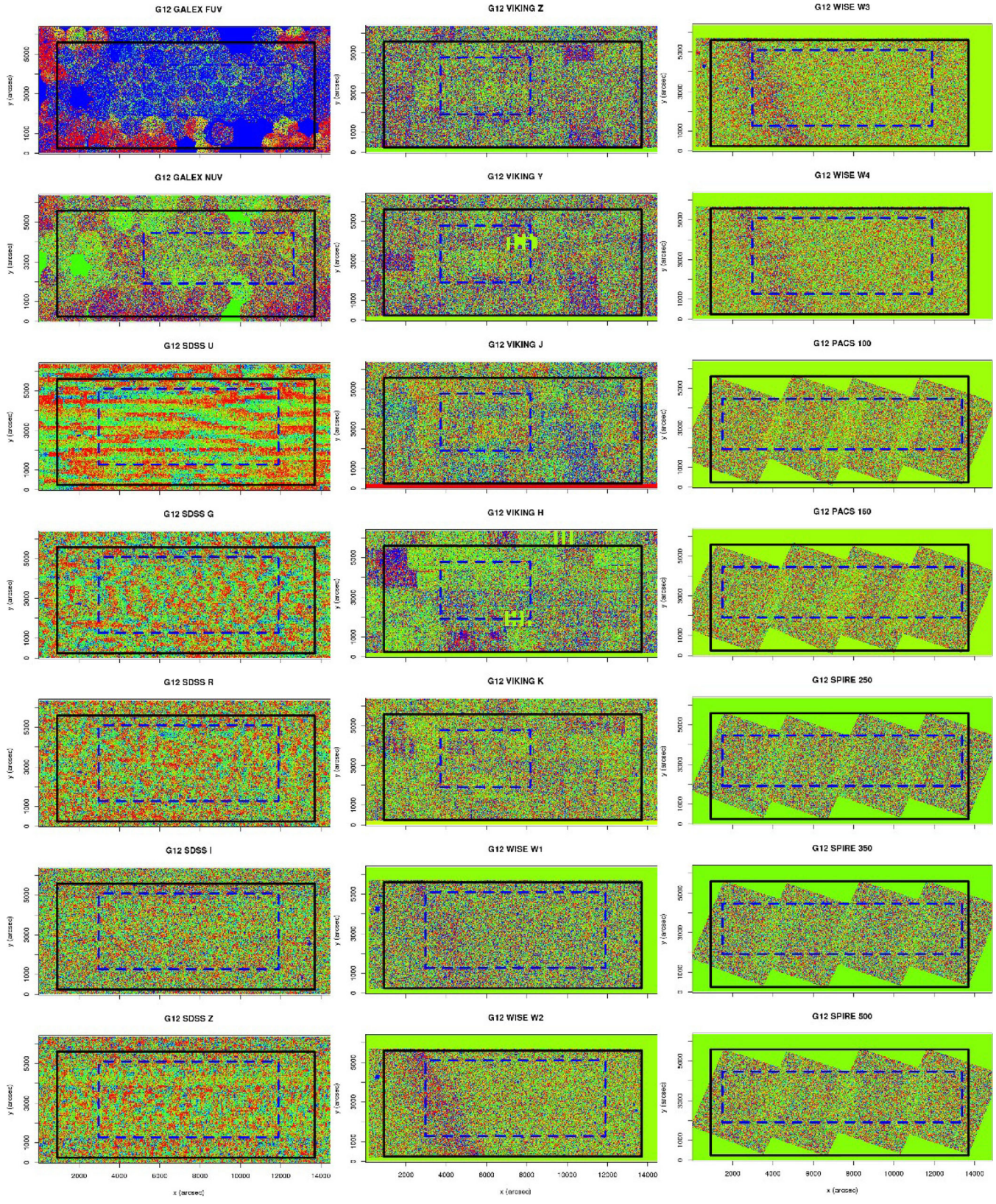

Figure A2. Background uniformity and coverage in the G12 region for *GALEX*, SDSS, VIKING, *WISE,* and *Herschel* data.

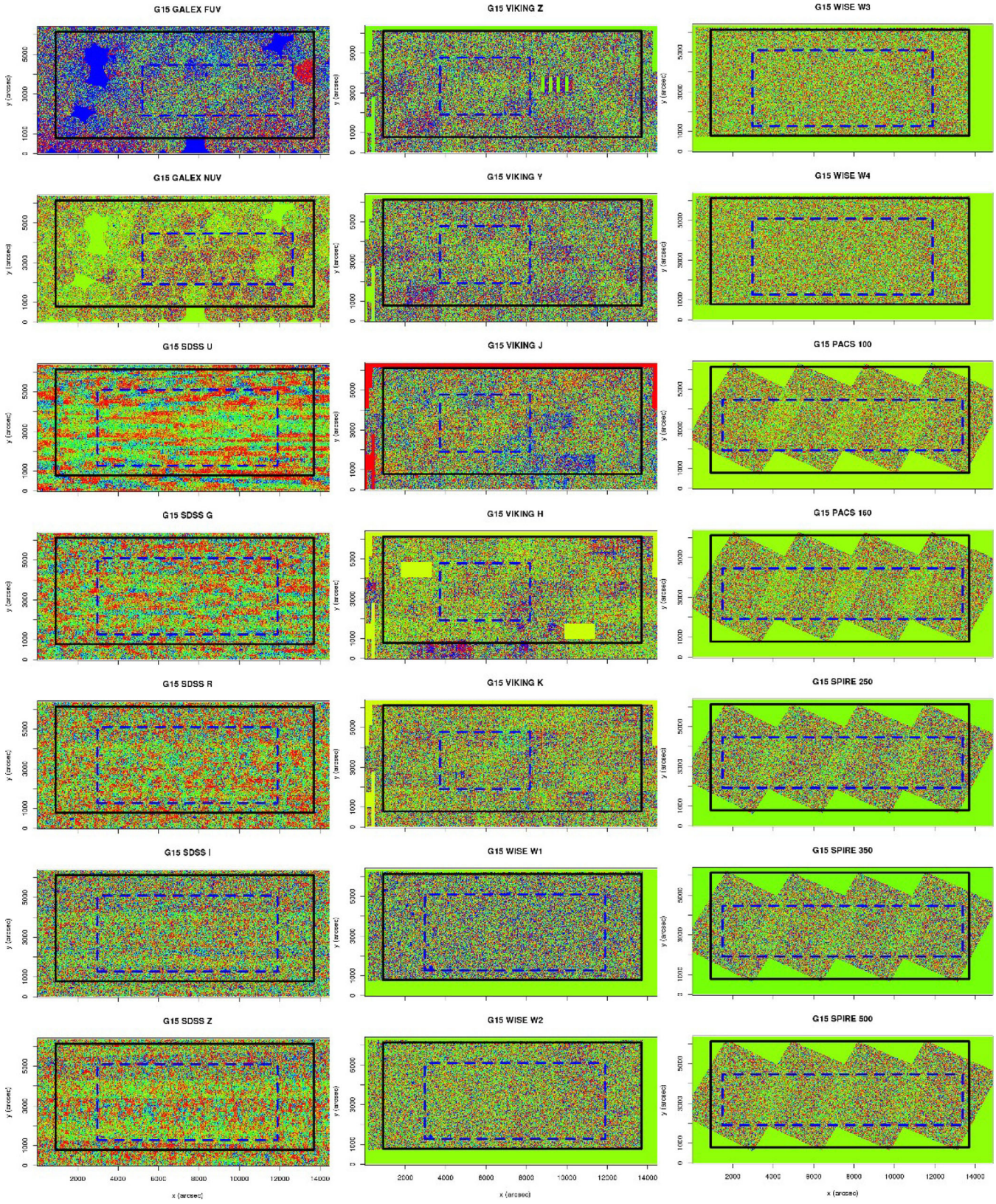

Figure A3. Background uniformity and coverage in the G15 region for *GALEX*, SDSS, VIKING, *WISE,* and *Herschel* data.

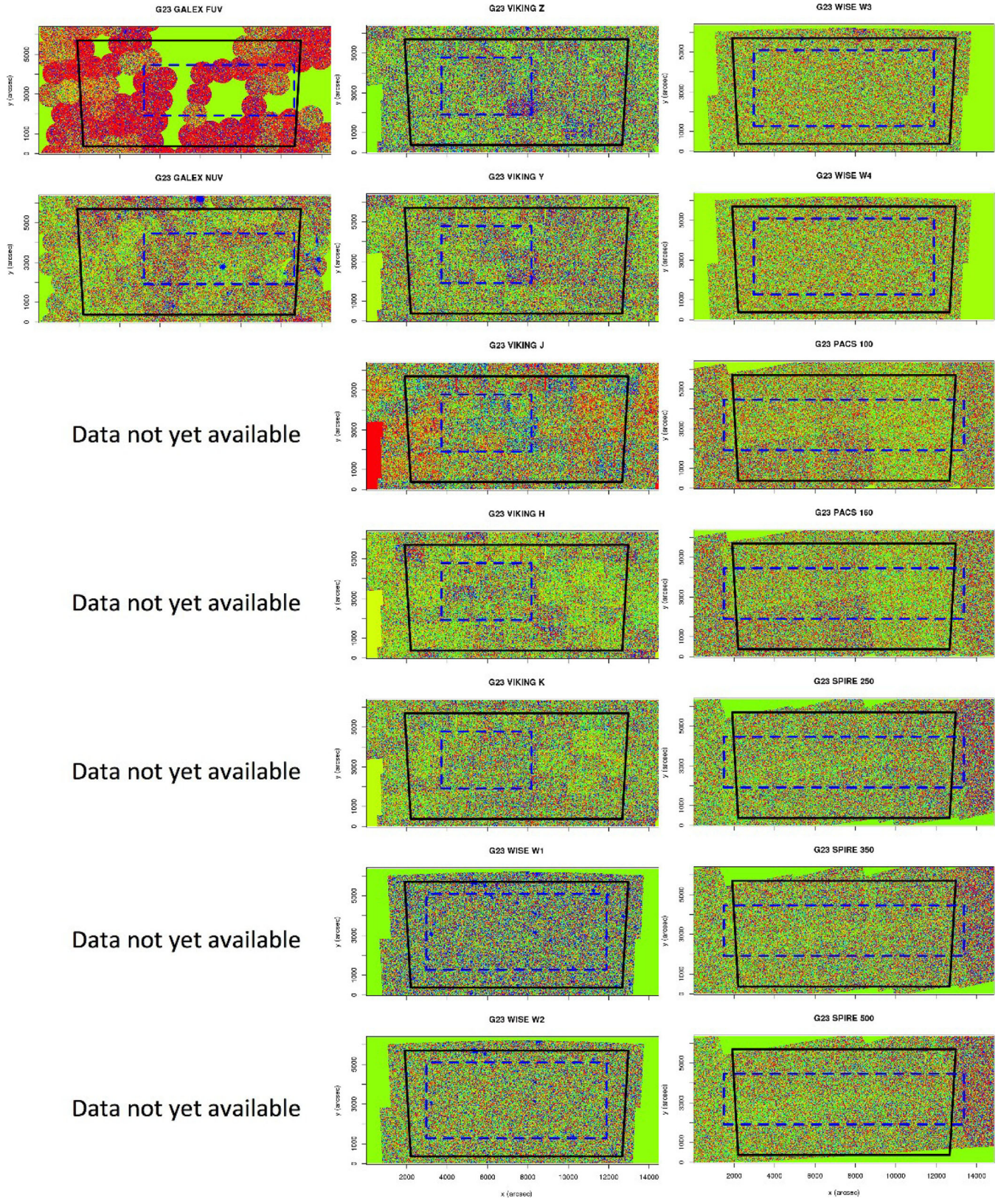

Figure A4. Background uniformity and coverage in the G23 region for *GALEX*, VIKING, *WISE,* and *Herschel* data.

[1]*International Centre for Radio Astronomy Research (ICRAR), The University of Western Australia, 35 Stirling Highway, Crawley, WA 6009, Australia*
[2]*SUPA, (Scottish Universities Physics Alliance), School of Physics & Astronomy, University of St Andrews, North Haugh, St Andrews KY16 9SS, UK*
[3] *NASA Ames Research Centre, N232, Moffett Field, Mountain View, CA 94035, United States*
[4]*Max Planck Institute for Nuclear Physics (MPIK), Saupfercheckweg 1, D-69117 Heidelberg, Germany*
[5]*Astrophysics Research Institute, Liverpool John Moores University, IC2, Liverpool Science Park, 146 Brownlow Hill, Liverpool L3 5RF, UK*
[6]*Australian Astronomical Observatory, PO Box 915, North Ryde, NSW 1670, Australia*
[7]*Centre for Astronomy and Particle Theory, University of Nottingham, University Park, Nottingham NG7 2RD, UK*
[8]*Sydney Institute for Astronomy, School of Physics, University of Sydney, NSW 2006, Australia*
[9]*SUPA, Institute for Astronomy, University of Edinburgh, Royal Observatory, Blackford Hill, Edinburgh EH9 3HJ, UK*
[10]*School of Physics, Monash University, Clayton, VIC 3800, Australia*
[11]*Astrophysics Group, The University of Western Cape, Robert Sobukwe Road, Bellville 7530, South Africa*
[12]*Research School of Astronomy and Astrophysics, Australian National University, Canberra, ACT 2611, Australia*
[13]*Centre for Astrophysics and Supercomputing, Swinburne University of Technology, Hawthorn, VIC 3122, Australia*
[14]*Finnish Centre for Astronomy with ESO, University of Turku, Väisäläntie 20, Piikkiö FI-21500, Finland*
[15]*School of Mathematics and Physics, University of Queensland, Brisbane, QLD 4072, Australia*
[16]*School of Physics and Astronomy, Cardiff University, Queens Buildings, The Parade, Cardiff CF24 3AA, UK*
[17]*Centre for Extragalactic Astronomy, Department of Physics, Durham University, South Road, Durham DH1 3LE, UK*
[18]*Institute for Computational Cosmology, Department of Physics, Durham University, South Road, Durham DH1 3LE, UK*
[19]*Leiden Observatory, University of Leiden, Niels Bohrweg 2, NL-2333 CA Leiden, the Netherlands*
[20]*Instituto de Física y Astronomía, Universidad de Valparaíso, Avda. Gran Bretaña 1111, Valparaíso, Chile*
[21]*European Southern Observatory, Karl-Schwarzschild-Str. 2, D-85748 Garching, Germany*
[22]*Department of Astronomy, University of Cape Town, Private Bag X3, Rondebosch 7701, South Africa*
[23]*Department of Physics and Astronomy, Macquarie University, Sydney, NSW 2109, Australia*
[24]*Instituto de Astronomía, Universidad Nacional Autómana de México, A.P. 70-264, 04510 México, D.F., México*
[25]*Hamburger Sternwarte, Universität Hamburg, Gojenbergsweg 112, D-21029 Hamburg, Germany*
[26]*Astronomy Centre, Department of Physics and Astronomy, University of Sussex, Falmer, Brighton BN1 9QH, UK*
[27]*Observatories of the Carnegie Institute for Science, 813 Santa Barbara Street, Pasadena, CA 91101, USA*
[28]*Indian Institute of Science Education and Research Mohali, Knowledge City, Sector 81, Manauli, 140306 Punjab, India*
[29]*Institute of Cosmology and Gravitation, University of Portsmouth, Dennis Sciama Building, Burnaby Road, Portsmouth PO1 3FX, UK*
[30]*Astrophysics Group, H.H. Wills Physics Laboratory, University of Bristol, Tyndall Avenue, Bristol BS8 1TL, UK*
[31]*Jeremiah Horrocks Institute, University of Central Lancashire, Preston, Lancashire PR1 2HE, UK*
[32]*Department of Physics and Mathematics & E.A.Milne Centre for Astrophysics, University of Hull, Cottingham Road, Kingston-upon-Hull HU6 7RX, UK*
[33]*Astronomy Unit, Queen Mary University London, Mile End Rd, London E1 4NS, UK*
[34]*School of Physics, The University of Melbourne, Parkville, VIC 3010, Australia*
[35]*SRON Netherlands Institute for Space Research, Landleven 12, NL-9747 AD Groningen, the Netherlands*

This paper has been typeset from a TEX/LATEX file prepared by the author.